National Library of Canada
Acquisitions and Bibliographic Services Branch
395 Wellington Street
Ottawa, Ontario
K1A 0N4

Bibliothèque nationale du Canada
Direction des acquisitions et des services bibliographiques
395, rue Wellington
Ottawa (Ontario)
K1A 0N4

Your file *Votre référence*

Our file *Notre référence*

NOTICE

The quality of this microform is heavily dependent upon the quality of the original thesis submitted for microfilming. Every effort has been made to ensure the highest quality of reproduction possible.

If pages are missing, contact the university which granted the degree.

Some pages may have indistinct print especially if the original pages were typed with a poor typewriter ribbon or if the university sent us an inferior photocopy.

Reproduction in full or in part of this microform is governed by the Canadian Copyright Act, R.S.C. 1970, c. C-30, and subsequent amendments.

AVIS

La qualité de cette microforme dépend grandement de la qualité de la thèse soumise au microfilmage. Nous avons tout fait pour assurer une qualité supérieure de reproduction.

S'il manque des pages, veuillez communiquer avec l'université qui a conféré le grade.

La qualité d'impression de certaines pages peut laisser à désirer, surtout si les pages originales ont été dactylographiées à l'aide d'un ruban usé ou si l'université nous a fait parvenir une photocopie de qualité inférieure.

La reproduction, même partielle, de cette microforme est soumise à la Loi canadienne sur le droit d'auteur, SRC 1970, c. C-30, et ses amendements subséquents.

Canada

University of Alberta

STUDIES OF HOT ALUMINUM SPUTTER DEPOSITION FOR MICROELECTRONICS PROCESSING

BY

Marcos Chun Wing Lam

A thesis submitted to the Faculty of Graduate Studies and Research in Partial fulfillment of the requirements for the degree of **MASTER OF SCIENCE**

DEPARTMENT OF **ELECTRICAL ENGINEERING**

Edmonton, Alberta

FALL 1994

National Library of Canada
Acquisitions and Bibliographic Services Branch
395 Wellington Street
Ottawa, Ontario
K1A 0N4

Bibliothèque nationale du Canada
Direction des acquisitions et des services bibliographiques
395, rue Wellington
Ottawa (Ontario)
K1A 0N4

Your file Votre référence

Our file Notre référence

The author has granted an irrevocable non-exclusive licence allowing the National Library of Canada to reproduce, loan, distribute or sell copies of his/her thesis by any means and in any form or format, making this thesis available to interested persons.

L'auteur a accordé une licence irrévocable et non exclusive permettant à la Bibliothèque nationale du Canada de reproduire, prêter, distribuer ou vendre des copies de sa thèse de quelque manière et sous quelque forme que ce soit pour mettre des exemplaires de cette thèse à la disposition des personnes intéressées.

The author retains ownership of the copyright in his/her thesis. Neither the thesis nor substantial extracts from it may be printed or otherwise reproduced without his/her permission.

L'auteur conserve la propriété du droit d'auteur qui protège sa thèse. Ni la thèse ni des extraits substantiels de celle-ci ne doivent être imprimés ou autrement reproduits sans son autorisation.

ISBN 0-315-95063-3

Canada

September 26, 1994

To whom it may concern,

Permission is hereby granted to Marcos Chun-Wing Lam to reproduce copies of Figure 1.5 which appears on page 9 of my Ph.D. thesis entitled "Thin Film Microstructure Effects in VLSI Metallization", which was accepted by the Faculty of Graduate Studies and Research at the University of Alberta on March 3, 1992. Permission is granted to reproduce copies for private, scholarly or scientific research purposes only.

Sincerely

R.N. Tait
Research Scientist
Alberta Microelectronic Centre
#318 11315 87 Avenue
Edmonton, Alberta
Canada T6G 2T9
phone: (403) 492 3914
fax: (403) 492 1643

Name Marcos Lam

Dissertation Abstracts International is arranged by broad, general subject categories. Please select the one subject which most nearly describes the content of your dissertation. Enter the corresponding four-digit code in the spaces provided.

Electronics and Electrical Engineering — SUBJECT TERM

0544 — SUBJECT CODE

U·M·I

Subject Categories

THE HUMANITIES AND SOCIAL SCIENCES

COMMUNICATIONS AND THE ARTS
- Architecture ... 0729
- Art History ... 0377
- Cinema ... 0900
- Dance ... 0378
- Fine Arts ... 0357
- Information Science ... 0723
- Journalism ... 0391
- Library Science ... 0399
- Mass Communications ... 0708
- Music ... 0413
- Speech Communication ... 0459
- Theater ... 0465

EDUCATION
- General ... 0515
- Administration ... 0514
- Adult and Continuing ... 0516
- Agricultural ... 0517
- Art ... 0273
- Bilingual and Multicultural ... 0282
- Business ... 0688
- Community College ... 0275
- Curriculum and Instruction ... 0727
- Early Childhood ... 0518
- Elementary ... 0524
- Finance ... 0277
- Guidance and Counseling ... 0519
- Health ... 0680
- Higher ... 0745
- History of ... 0520
- Home Economics ... 0278
- Industrial ... 0521
- Language and Literature ... 0279
- Mathematics ... 0280
- Music ... 0522
- Philosophy of ... 0998
- Physical ... 0523
- Psychology ... 0525
- Reading ... 0535
- Religious ... 0527
- Sciences ... 0714
- Secondary ... 0533
- Social Sciences ... 0534
- Sociology of ... 0340
- Special ... 0529
- Teacher Training ... 0530
- Technology ... 0710
- Tests and Measurements ... 0288
- Vocational ... 0747

LANGUAGE, LITERATURE AND LINGUISTICS
- Language
  - General ... 0679
  - Ancient ... 0289
  - Linguistics ... 0290
  - Modern ... 0291
- Literature
  - General ... 0401
  - Classical ... 0294
  - Comparative ... 0295
  - Medieval ... 0297
  - Modern ... 0298
  - African ... 0316
  - American ... 0591
  - Asian ... 0305
  - Canadian (English) ... 0352
  - Canadian (French) ... 0355
  - English ... 0593
  - Germanic ... 0311
  - Latin American ... 0312
  - Middle Eastern ... 0315
  - Romance ... 0313
  - Slavic and East European ... 0314

PHILOSOPHY, RELIGION AND THEOLOGY
- Philosophy ... 0422
- Religion
  - General ... 0318
  - Biblical Studies ... 0321
  - Clergy ... 0319
  - History of ... 0320
  - Philosophy of ... 0322
- Theology ... 0469

SOCIAL SCIENCES
- American Studies ... 0323
- Anthropology
  - Archaeology ... 0324
  - Cultural ... 0326
  - Physical ... 0327
- Business Administration
  - General ... 0310
  - Accounting ... 0272
  - Banking ... 0770
  - Management ... 0454
  - Marketing ... 0338
- Canadian Studies ... 0385
- Economics
  - General ... 0501
  - Agricultural ... 0503
  - Commerce-Business ... 0505
  - Finance ... 0508
  - History ... 0509
  - Labor ... 0510
  - Theory ... 0511
- Folklore ... 0358
- Geography ... 0366
- Gerontology ... 0351
- History
  - General ... 0578
  - Ancient ... 0579
  - Medieval ... 0581
  - Modern ... 0582
  - Black ... 0328
  - African ... 0331
  - Asia, Australia and Oceania ... 0332
  - Canadian ... 0334
  - European ... 0335
  - Latin American ... 0336
  - Middle Eastern ... 0333
  - United States ... 0337
- History of Science ... 0585
- Law ... 0398
- Political Science
  - General ... 0615
  - International Law and Relations ... 0616
  - Public Administration ... 0617
- Recreation ... 0814
- Social Work ... 0452
- Sociology
  - General ... 0626
  - Criminology and Penology ... 0627
  - Demography ... 0938
  - Ethnic and Racial Studies ... 0631
  - Individual and Family Studies ... 0628
  - Industrial and Labor Relations ... 0629
  - Public and Social Welfare ... 0630
  - Social Structure and Development ... 0700
  - Theory and Methods ... 0344
- Transportation ... 0709
- Urban and Regional Planning ... 0999
- Women's Studies ... 0453

THE SCIENCES AND ENGINEERING

BIOLOGICAL SCIENCES
- Agriculture
  - General ... 0473
  - Agronomy ... 0285
  - Animal Culture and Nutrition ... 0475
  - Animal Pathology ... 0476
  - Food Science and Technology ... 0359
  - Forestry and Wildlife ... 0478
  - Plant Culture ... 0479
  - Plant Pathology ... 0480
  - Plant Physiology ... 0817
  - Range Management ... 0777
  - Wood Technology ... 0746
- Biology
  - General ... 0306
  - Anatomy ... 0287
  - Biostatistics ... 0308
  - Botany ... 0309
  - Cell ... 0379
  - Ecology ... 0329
  - Entomology ... 0353
  - Genetics ... 0369
  - Limnology ... 0793
  - Microbiology ... 0410
  - Molecular ... 0307
  - Neuroscience ... 0317
  - Oceanography ... 0416
  - Physiology ... 0433
  - Radiation ... 0821
  - Veterinary Science ... 0778
  - Zoology ... 0472
- Biophysics
  - General ... 0786
  - Medical ... 0760

EARTH SCIENCES
- Biogeochemistry ... 0425
- Geochemistry ... 0996
- Geodesy ... 0370
- Geology ... 0372
- Geophysics ... 0373
- Hydrology ... 0388
- Mineralogy ... 0411
- Paleobotany ... 0345
- Paleoecology ... 0426
- Paleontology ... 0418
- Paleozoology ... 0985
- Palynology ... 0427
- Physical Geography ... 0368
- Physical Oceanography ... 0415

HEALTH AND ENVIRONMENTAL SCIENCES
- Environmental Sciences ... 0768
- Health Sciences
  - General ... 0566
  - Audiology ... 0300
  - Chemotherapy ... 0992
  - Dentistry ... 0567
  - Education ... 0350
  - Hospital Management ... 0769
  - Human Development ... 0758
  - Immunology ... 0982
  - Medicine and Surgery ... 0564
  - Mental Health ... 0347
  - Nursing ... 0569
  - Nutrition ... 0570
  - Obstetrics and Gynecology ... 0380
  - Occupational Health and Therapy ... 0354
  - Ophthalmology ... 0381
  - Pathology ... 0571
  - Pharmacology ... 0419
  - Pharmacy ... 0572
  - Physical Therapy ... 0382
  - Public Health ... 0573
  - Radiology ... 0574
  - Recreation ... 0575
  - Speech Pathology ... 0460
  - Toxicology ... 0383
- Home Economics ... 0386

PHYSICAL SCIENCES

Pure Sciences
- Chemistry
  - General ... 0485
  - Agricultural ... 0749
  - Analytical ... 0486
  - Biochemistry ... 0487
  - Inorganic ... 0488
  - Nuclear ... 0738
  - Organic ... 0490
  - Pharmaceutical ... 0491
  - Physical ... 0494
  - Polymer ... 0495
  - Radiation ... 0754
- Mathematics ... 0405
- Physics
  - General ... 0605
  - Acoustics ... 0986
  - Astronomy and Astrophysics ... 0606
  - Atmospheric Science ... 0608
  - Atomic ... 0748
  - Electronics and Electricity ... 0607
  - Elementary Particles and High Energy ... 0798
  - Fluid and Plasma ... 0759
  - Molecular ... 0609
  - Nuclear ... 0610
  - Optics ... 0752
  - Radiation ... 0756
  - Solid State ... 0611
- Statistics ... 0463

Applied Sciences
- Applied Mechanics ... 0346
- Computer Science ... 0984
- Engineering
  - General ... 0537
  - Aerospace ... 0538
  - Agricultural ... 0539
  - Automotive ... 0540
  - Biomedical ... 0541
  - Chemical ... 0542
  - Civil ... 0543
  - Electronics and Electrical ... 0544
  - Heat and Thermodynamics ... 0348
  - Hydraulic ... 0545
  - Industrial ... 0546
  - Marine ... 0547
  - Materials Science ... 0794
  - Mechanical ... 0548
  - Metallurgy ... 0743
  - Mining ... 0551
  - Nuclear ... 0552
  - Packaging ... 0549
  - Petroleum ... 0765
  - Sanitary and Municipal ... 0554
  - System Science ... 0790
- Geotechnology ... 0428
- Operations Research ... 0796
- Plastics Technology ... 0795
- Textile Technology ... 0994

PSYCHOLOGY
- General ... 0621
- Behavioral ... 0384
- Clinical ... 0622
- Developmental ... 0620
- Experimental ... 0623
- Industrial ... 0624
- Personality ... 0625
- Physiological ... 0989
- Psychobiology ... 0349
- Psychometrics ... 0632
- Social ... 0451

UNIVERSITY OF ALBERTA

RELEASE FORM

NAME OF AUTHOR: **Marcos Chun Wing Lam**

TITLE OF THESIS: **Studies of Hot Aluminum Sputter Deposition for Microelectronics Processing**

DEGREE: **Master of Science**

YEAR THIS DEGREE GRANTED: **Fall 1994**

Permission is hereby granted to the University of Alberta Library to reproduce single copies of this thesis and to lend or sell such copies for private, scholarly or scientific research purposes only.

The author reserves all other publication and other rights in association with the copyright in the thesis, and except as hereinbefore provided neither the thesis nor any substantial portion thereof may be printed or otherwise reproduced in any material form whatever without the author's prior written permission.

Marcos Lam c/o. Dr. Curtis Ling
EEE Department
Clear Water Bay Road
Clear Water Bay, Sai Kung
Hong Kong

Date : Oct. 7, 94

University of Alberta

FACULTY OF GRADUATE STUDIES AND RESEARCH

The undersigned certify that they have read, and recommend to the Faculty of Graduate Studies and Research for acceptance, a thesis entitled STUDIES OF HOT ALUMINUM SPUTTER DEPOSITION FOR MICROELECTRONICS PROCESSING submitted by MARCOS CHUN WING LAM in partial fulfillment of the requirements for the degree of MASTER OF SCIENCE.

Dr. M. J. Brett
Supervisor

Dr. R.P.W. Lawson

Dr. R.F. Egerton

Dr. S.K. Dew

October 4,1994

Abstract

This thesis reports the investigation of the properties of high temperature sputtered aluminum for microelectronics applications. Aluminum films were deposited by a 1-step process with substrate temperature fixed, and a 3-step process with a heating sequence of no heating, temperature ramping, and hot. The films were characterized in terms of their grain sizes, crystal orientation, and coverage over topography. Also, film growth was simulated utilizing two models, namely, SIMSPUD and SIMBAD. From the 1-step method, the aluminum film properties critical to electromigration resistance improved as the substrate temperatures increased to a maximum of 550 °C. These improved properties included a larger grain size, strong <111> crystal orientation, better coverage over topography, and were the result of an increased adatom diffusion length at higher temperatures. The 3-step process improved coverage in some regions, but was inconsistent over a die. Outgassing and lack of sustained baking were believed to be the cause of the inconsistency for the 3-step process.

This thesis has provided the first experimental verification of the SIMBAD model for high temperature sputtered aluminum. SIMBAD successfully predicted the film profile for high temperature films. The surface diffusion length constant $\sqrt{D_0\tau}$ and activation energy Q_s for diffusion were inferred from a comparison of simulation and experiment and found to be 38 μm and 0.59 eV, respectively.

To Candy Law

Acknowledgment

I would like to thank my supervisor, Dr. Brett for his guidance, encouragement and support throughout this research. I would also like to thank Dr. Dew for his suggestions on simulation. I sincerely thank Dr. Liu for his support as a colleague and a friend. I would like to thank Graham McKinnon and Glen Fitzpatrick for their technical support.

Finally, I also thank the Alberta Microelectronic Centre for its financial assistance and research facilities.

Table of Contents

CHAPTER 1 : INTRODUCTION 1

1.1 Review of the State-of-the-Art and the Requirements of Metallization 1

1.1.1 Electromigration 3

1.1.2 Sputtering 6

1.1.3 Sputtered Film Characteristics 8

1.1.3 Coverage 11

1.2 Emerging Techniques 15

1.2.1 Bias Sputtering 15

1.2.2 Laser Irradiation 16

1.2.3 Tungsten Plugs 16

1.2.4 High Temperature Sputtering 18

1.3 Simulation 19

CHAPTER 2 : EXPERIMENTAL SETUP AND PROCEDURE 21

2.1 System Requirements and Specifications 21

2.2 Setup of the UHV System 23

2.2.1 Loadlock 23

2.2.2 Substrate Heating and Baking 24

2.2.3 Cold Shroud 26

2.2.4 Sputtering Chamber 26

2.2.5 Basic Sputtering Equipment 27

2.2.6 Leak Checking and System Performance 28

2.3 Estimation of Background Gas Pressure during Deposition 29

2.4 Deposition Procedures 33

2.4.1 Substrates and Their Preparation 33

2.4.2 Baking and Sample Loading 35

2.4.3 1-step Deposition Experiments 36

2.4.4 3-step Deposition Experiment 37

CHAPTER 3 : EXPERIMENTAL RESULTS 41

3.1 1-step Deposition Process 41

3.1.1 Coverage 41

3.1.2 Surface Curvature 45

3.1.3 Grain Size 48

3.1.4 Crystal Orientation 51

3.1.5 Stress 54

3.1.5 Summary 58

3.2 3-Step Deposition 59

3.3 2- and 3-dimensional Effects 62

3.5 Summary 64

CHAPTER 4 : SIMULATIONS 65

4.1 Sputter Flux Simulation 65

4.2 Film Growth Simulation 67

4.3 Extraction of Simulation Parameters 69

4.3.1 Target Erosion Profile 69

4.3.2 Collision Cross-section 70

4.3.3 Sticking Coefficient 71

4.4 Angular Distribution 74

4.5 1-step Deposited Film Simulation 78

CHAPTER 5 : CONCLUSION **84**

REFERENCES **86**

List of Tables

1.1 Diffusion Length of Dopants 19

2.1 Specifications of the UHV Sputtering System 23

2.2 1-Step Deposition Procedures 38

2.3 3-Step Deposition Parameters 40

3.1 Coverages on Trenches 44

3.2 XRD Peak Identification 51

3.3 Film Stress 57

List of Figures

1.1 Four-Level Metallization Structure. 2

1.2 Magnetron Sputtering 7

1.3 Structure-Zone Models 9

1.4 Illustration of Film Growth 10

1.5 Definition of Bottom and Step Coverages 12

1.6 Sputtered Aluminum on Oxide Steps 12

1.7 Flux Acceptance Angle vs. Trench Width 14

2.1 Schematic of the UHV Sputtering System 22

2.2 Overhang Structure 34

2.3 Hot Aluminum Film Growth Sequence 39

3.1 Aluminum Sputtered on Trenches 42

3.2 Effect of Diffusion Length on Surface Curvature 46

3.3 Radius of Curvature vs. Deposition Temperature 47

3.4 Top Views of Aluminum Films 49

3.5 Grain Size vs. Deposition Temperature 50

3.6 XRD Scan of RT Film 52

3.7 Expanded XRD Scans of Aluminum Films 52

3.8 Compresseively Stressed Film on Top of an Overhang 55

3.9 Aluminum Films Deposited on Overhang Structures 55

3.10 Aluminum deposited on Trenches by 1-Step and 3-Step Methods 61

3.11 Aluminum Deposited on Vias by 1-Step and 3-Step Methods 64

4.1 SIMSPUD Simulation Sequence 67

4.2 SIMBAD Simulation Sequence 68

4.3 Erosion Profile 71

4.4 High Magnification Micrograph of Aluminum Film on an Overhang 73

4.5 Effect of Sticking Coefficients 74

4.6 Simulated Angular Distributions 76

4.7 Relative Flux Acceptance vs. Trench Width 79

4.8 Simulation of Sputtered Aluminum Films 80

4.9 Surface Diffusion Length vs. Substrate Temperature 81

List of Symbols

MTF	- Mean Time to Failure
J	- current density
Q	- activation energy
$k_B T$	- thermal energy
T_m	- melting temperature
RC	- propagation time delay
ρ	- resistivity
t_m	- metal film thickness
l	- length of interconnect
k	- dielectric constant
t_{ox}	- oxide film thickness
P_{base}	- base pressure
P_{ig}, P_w, P_{out}	- partial pressures of impurity gas, working gas, and outgassing
P_{cryo}, P_{cold}	- base pressures achieved by cryopump and cold shroud
Q_{out}, Q_w	- outgassing rate and working gas flow rate
S_{sys}, S_w	- normal pumping speed and pumping speed during sputtering

S_{cryo}, S_{cold}	- pumping speeds achieved by cryopump and cold shroud
d	- average grain diameter
n	- number of grains per mm^2
s	- film stress
δ	- displacement at the end of an overhang
E	- Young's modulus
t	- film thickness
ν	- Poisson's ratio
μ, μ_0	- surface potentials of a 2-dimensional surface and a flat surface
γ	- surface tension
R	- radius of curvature
RT	- Room Temperature
Ω	- atomic volume
L	- surface diffusion length
D_0	- intrinsic diffusivity
τ	- mean adatom lifetime
Q_s	- activation energy for surface diffusion

σ - collision cross-section

η - relative flux acceptance

Φ - angular distribution

θ_a - acceptance angle

Chapter 1 : Introduction

Over the last three decades, integrated circuit (IC) technology has advanced significantly towards smaller feature size, higher packing density, and larger die size. Many technical difficulties during IC fabrication have been encountered. One of the most difficult problems is depositing effective metallization to provide conducting paths between devices. Because of the reduction in lateral dimensions, the conventional metallization technique, sputtering, is unable to provide sufficiently uniform coverage over extreme topographies, such as high aspect ratio (depth:width) vias and trenches. Inadequate coverage may lead to interconnect failure by electromigration or stress-induced voiding. This is especially true at the high current densities associated with smaller dimensions. Therefore, new metallization techniques are emerging to overcome the deficiencies of conventional sputtering. By experiment and simulation, this thesis investigates one of the new metallization techniques, high-temperature aluminum sputtering.

1.1 Review of the State-of-the-Art and the Requirements of Metallization

To facilitate the demands for higher functionality and larger data storage, more and more devices are being packed into a single integrated circuit (IC) chip. The current generation of IC's, utilizing ultra large scale integration (ULSI), has more than 10 million transistors on a chip and has feature sizes less than 1 μm [1,2]. As a result of the high packing density, the amount of area consumed by interconnections often exceeds the

area occupied by devices [3,4]. Multi-level metallization schemes are being employed to stack up metallization layers vertically in order to utilize die areas effectively [3,5]. A schematic drawing of a four level metallization structure is shown in Figure 1.1. The added levels complicate and lengthen the processing sequence because each additional layer requires a similar number of processing steps as a single layer.

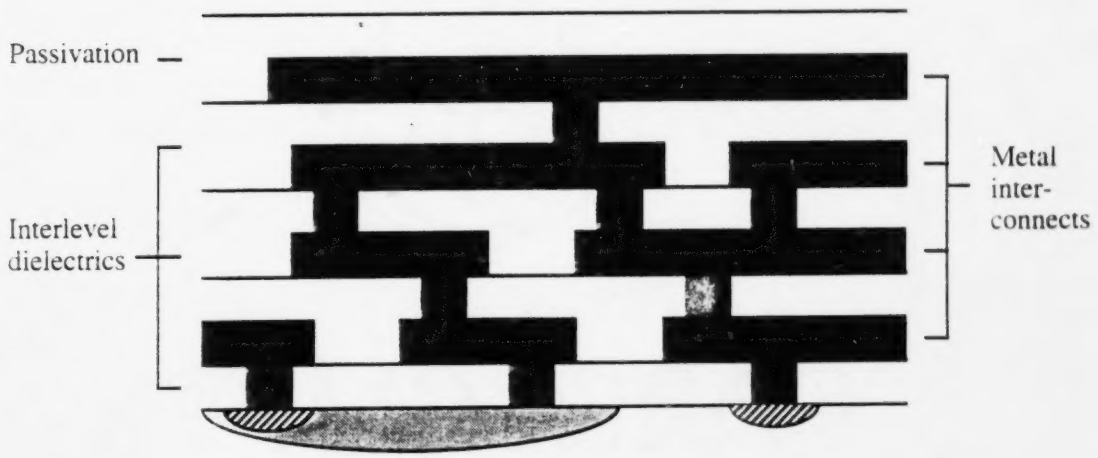

Figure 1.1 Cross-sectional view of a generalized four-level metallization structure [5]

The increased number of processing steps has a direct impact on the manufacturer's yield. The total yield of a complete IC process is equal to the product of the yield of each individual processing step :

$$\text{Yield} = \text{Yield}_1 \cdot \text{Yield}_2 \cdot \text{Yield}_3 \cdot \cdots \text{Yield}_n \qquad (1\text{-}1)$$

Here, the subscripts denote successive processing steps. The final yield is diminished as

more steps are involved. Thus, complicated metallization methods are not recommended on the basis of yield optimization.

Another important issue in aluminum-based metallization is electromigration. Electromigration is an electron current-induced diffusion of material along a metal line. When electron current is passed through a metal line, the collisions of the electrons with positive metal ions push material away from the anode toward the cathode of the wire. As long as the migration of material is uniform across the wire, no damage will occur in the metal line. However, the inhomogeneous grain-boundary structure of sputtered metal films disrupts the flow of material. Consequently, material is preferentially removed at some locations, forming voids, and accumulated at others, forming hillocks [6,7]. A more detailed discussion of electromigration is in Section 1.1.1.

As the features on IC's become smaller, less material is able to be deposited into vias and trenches by conventional sputtering techniques. The insufficient metal coverage over the vias and trenches escalates the problem of electromigration. Issues of deposition and coverage will be presented in Sections 1.1.2 and 1.1.3, respectively.

1.1.1 Electromigration

Electromigration was first identified as one of the failure mechanisms for metallization in the mid-1960s [8]. With feature sizes reduced by 30-fold since that time, electromigration is becoming the primary failure mode of metallization. The resistance to electromigration is commonly evaluated by the quantity mean time to failure (MTF) which is related empirically to the current density and temperature by [8]:

$$MTF \propto J^{-n} \exp\left(\frac{Q}{k_B T}\right) \tag{1.2}$$

where J is the current density, n is an exponent between 1 and 3, Q is the activation energy, k_B is Boltzmann's constant, and T is the absolute temperature.

Increased current density, associated with reduced feature size, escalates the problem of electromigration. A further complication is the poor heat dissipation of the multilevel metallization structure. The metallization is usually encapsulated by insulating dielectrics which have low thermal conductivities and are located at a distance from the heat-sunk substrate. The encapsulation hinders heat dissipation and results in elevated temperature of the metal lines [9, 10]. Proper consideration of thermal management is necessary when designing four- and five-level metallizations.

A small line width and poor metallization coverage are other factors affecting electromigration lifetime. The increase of the current density is inversely proportional to the line width. Thus, the MTF decreases with decreasing line width. In addition to narrower line width, the nonconformal coverage of a metal film over features enhances the current density at the thin regions, such as the side-walls of an oxide step. The ohmic loss is larger at the thin region because of higher electrical resistivity. Therefore, the local temperature is elevated with respect to other regions [10, 11, 12]. The larger current density and higher temperature at the thin region enhance the electromigration phenomenon. A better metallization technique for providing improved coverage is necessary to ensure the advancement of the microelectronics in the directions of high functionality and reliability.

In addition to film coverage, the grain size, crystal orientation, and alloy composition have great influence on the electromigration resistance of aluminum films. Grain boundary diffusion has been identified as the dominant transport mechanism for electromigration [13]. Since the grain boundaries per volume for larger grain films is less than that for finer grain films, the finer grain films have lower electromigration resistance [14, 15]. When the grain size is larger than the width of the metal lines, grain boundaries are often oriented across metal lines rather than along the lines. This 'bamboo structure' eliminates the effect of grain boundary diffusion along the direction of electron flow. Hence, bamboo structures increase the MTF [14, 16, 17]. It has also been found that the MTF of strong <111> oriented films is longer than that of randomly oriented films [4]. The randomness of crystal orientation re-enforces the divergence of material transport that ultimately leads to electromigration failures. Another important factor affecting electromigration is that aluminum films alloyed with a small percentage of a transition metal show an improved MTF. The most widely used alloying metal is copper, but many other metals, such as Ti, Pb, Sc, Nb, and Mg also show improvements in MTF for aluminum films [18].

In summary, electromigration failure rises from a flow of material under the influence of electron current. High current flow and any non-uniformity in the aluminum films will accelerate the process of electromigration. The desired qualities of aluminum films that resist electromigration are uniform coverage, large grain size, and strong <111> orientation.

1.1.2 Sputtering

Sputtering is the most widely used metallization technique and is a well-developed process with a variety of configurations [19, 20]. The most popular configuration is DC magnetron sputtering (See Figure 1.2 for a schematic diagram of this process). During operation, a working gas, typically argon, is injected into an evacuated chamber to create a partial vacuum and sustain a glow discharge. The discharge is ignited by an applied DC voltage to the cathode. This voltage ranges from tens to hundreds of volts. The discharge creates positively ionized gas particles in the plasma which are accelerated toward the negatively biased target. The target is the source of coating material and is mounted on the cathode. The bombardment of the target by energetic ions causes ejection of target material. The ejected material is intercepted by a substrate which is placed in front of the target.

The major distinction of magnetron sputtering over other configurations is the magnet located behind the target. The magnetic field confines the plasma near the target; therefore, the plasma can be ignited at a relatively low voltage and operated efficiently relative to other sputtering systems without magnets [20, 21]. The confinement of the plasma enhances the erosion and the ejection of sputtered material. Due to the localized erosion, a circular magnetron sputtering source would produce a ring of deposition flux. Because of the large area in sputtering compared to the point-like source in evaporation, the depositing flux reaches the substrate with a wider angular distribution. The spread of

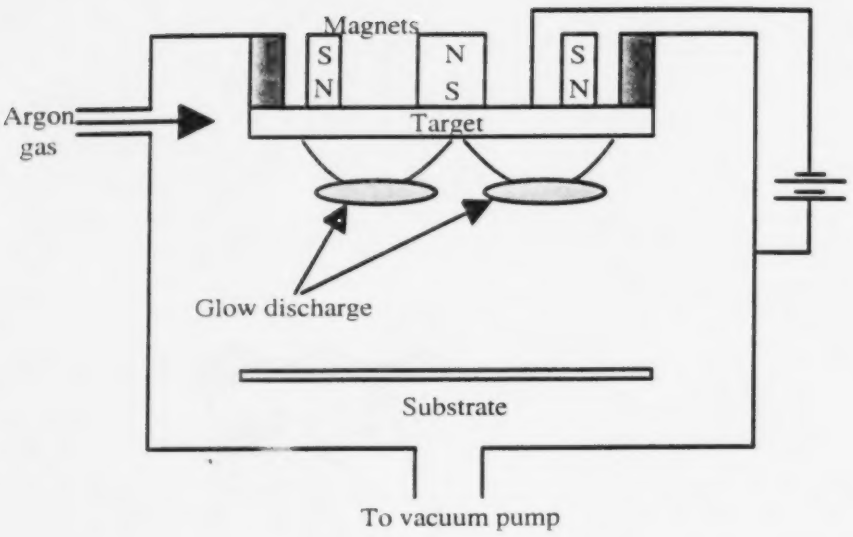

(a)

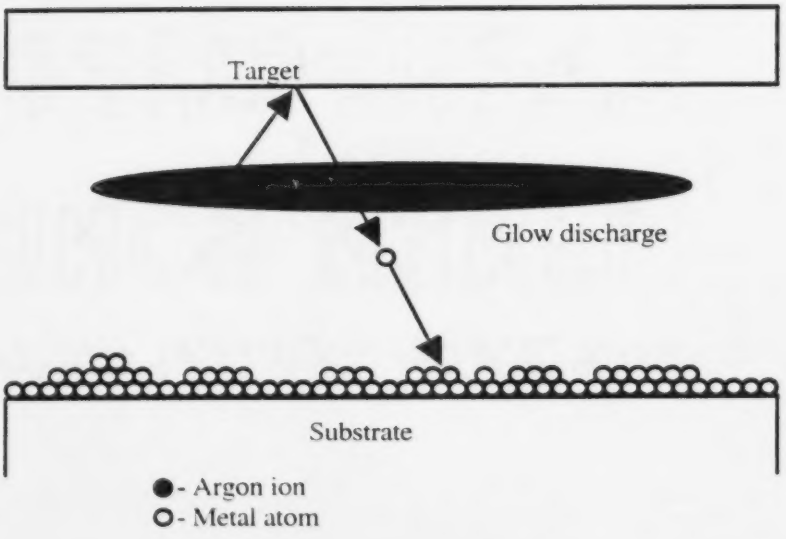

(b)

Figure 1.2 A schematic diagram of magnetron sputtering a) equipment and b) process

sputtered flux is further enhanced by collisions with the working gas during transport from the target to the substrate. Thus, the angular distribution of the sputtered flux is also a strong function of the working gas pressure. The broad angular distribution of sputtered material provides for a better coverage over topography, such as oxide steps. For this reason evaporation, which has a very small spread of flux, was replaced by sputtering as a metallization technique [15, 19]. However, conventional sputtering still has difficulty filling narrow vias and trenches on today's ULSI IC's.

1.1.3 Sputtered Film Characteristics

The characteristics of sputtered films depend mainly on two parameters, sputtering pressure and deposition temperature. In 1974, Thornton extended the structure-zone model (SZM) [22-25], which was originally proposed by Movchan and Demichishin (MD) [26] for evaporation, to magnetron sputtering. Both SZM's are shown schematically in Figure 1.3. The MD model categorizes evaporated films into three groups based on the ratio of substrate temperature, T, to the melting point, T_m, of the material. A brief description of the film growth sequence for physical vapour deposition is illustrated in Figure 1.4 to help explain the effect of substrate temperature on film characteristics. The first step of the deposition is the transport of the depositing material from a source to a substrate. Any structure above the substrate may intercept the depositing flux and shadow the substrate from flux. After impact, the depositing atoms will diffuse a short distance before incorporation into the film. The surface diffusion

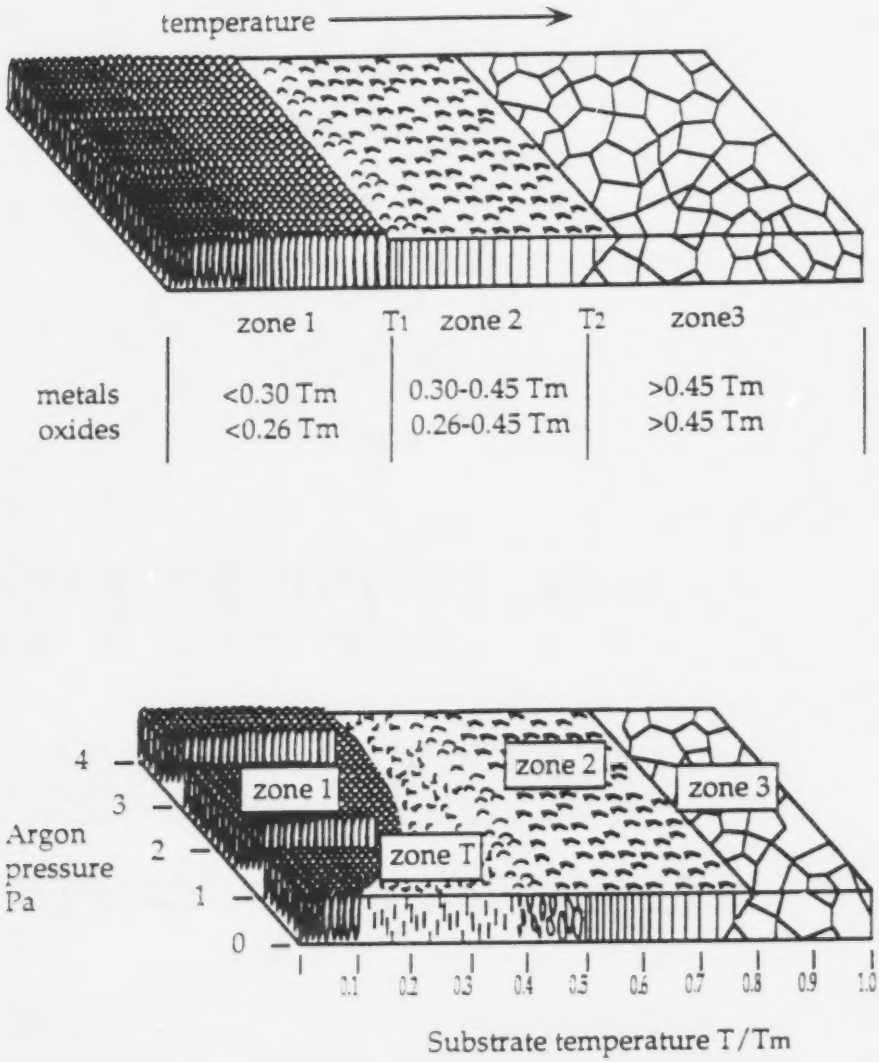

Figure 1.3 Structure-zone model for metal films deposited by a) evaporation and b) magnetron sputtering. (Figure used with permission of R.N. Tait. [27])

length increases monotonically with substrate temperature. On average, the adsorbed atom should finally bond at a location that has the lowest surface energy, thus material deposited at high surface energy areas (convex surfaces) would diffused to low surface energy areas (concave surfaces) and resulted in lower surface curvature on both convex and concave surfaces. In this manner, substrate temperatures have a great effect on the surface morphology of deposited films.

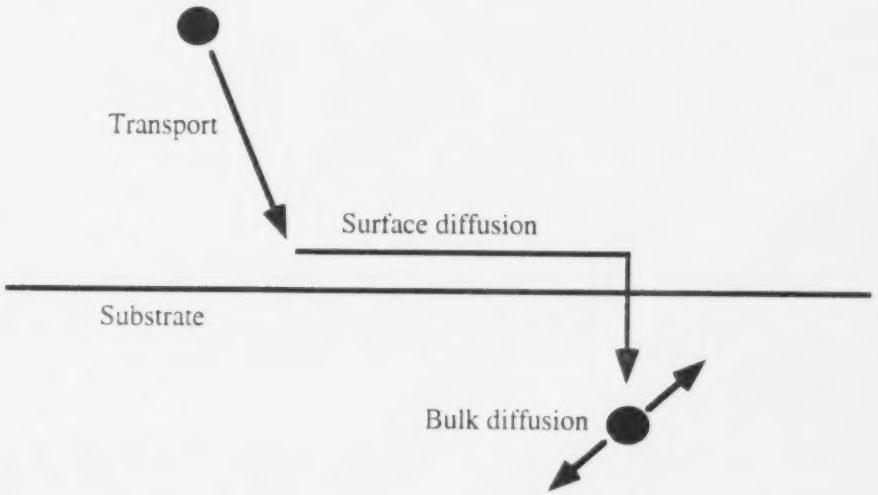

Figure 1.4 Schematic illustration of a film growth process by physical vapour deposition [24].

In the MD model, for low deposition temperature, $T/T_m < 0.3$, the surface diffusion of adsorbed atoms (adatoms) is insignificant so that the adatoms remain at the original impact site. Films deposited in this range of temperature are columnar and full of voids and are categorized as having zone 1 structure. Not shown in the MD model, the

angular distribution of vapour flux has a pronounced effect on the structures and properties of the zone 1 films. At higher temperatures, $0.3 < T/T_m < 0.45$, surface diffusion dominates and grains are well defined by grain boundaries. Because of the surface diffusion, the influence of the angular distribution of vapour flux is less. Bulk diffusion comes into effect for the zone 3 ($T/T_m > 0.45$) films. The grains are larger and smoother than those of the zone 2 films because of the long surface diffusion length.

Thornton extended the MD SZM to magnetron sputtering by including the effects of sputtering pressure and energetic species. An additional zone, called zone T, is included in the Thornton SZM and is an intermediate zone between zone 1 and zone 2. Since aluminum is a low melting material for which T/T_m is greater than 0.3 at room temperature, only zone 2 and zone 3 are of concern in this thesis.

1.1.3 Coverage

The coverage of a metal film over a trench is commonly evaluated by the terms step coverage and bottom coverage. These two quantities are defined in Figure 1.5 along with the aspect ratio. The bottom coverage is the ratio of the film thickness at the center of a trench bottom to the nominal film thickness. The step coverage is the ratio of the thickness at the thinnest region of the side-wall of the trench to the nominal thickness. In an ideal situation, these two ratios should be 100 percent. A scanning electron micrograph of a series of oxide steps coated with sputtered aluminum is shown in Figure 1.6. Most of the aluminum is deposited on the top of the oxide step, but only a small amount of aluminum is deposited on the side-wall and the bottom of the trenches. The

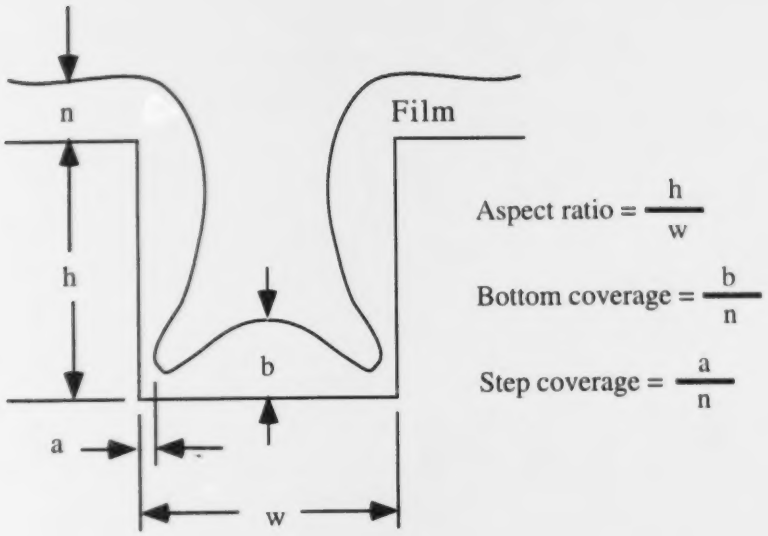

Figure 1.5 The definition of bottom and step coverages.

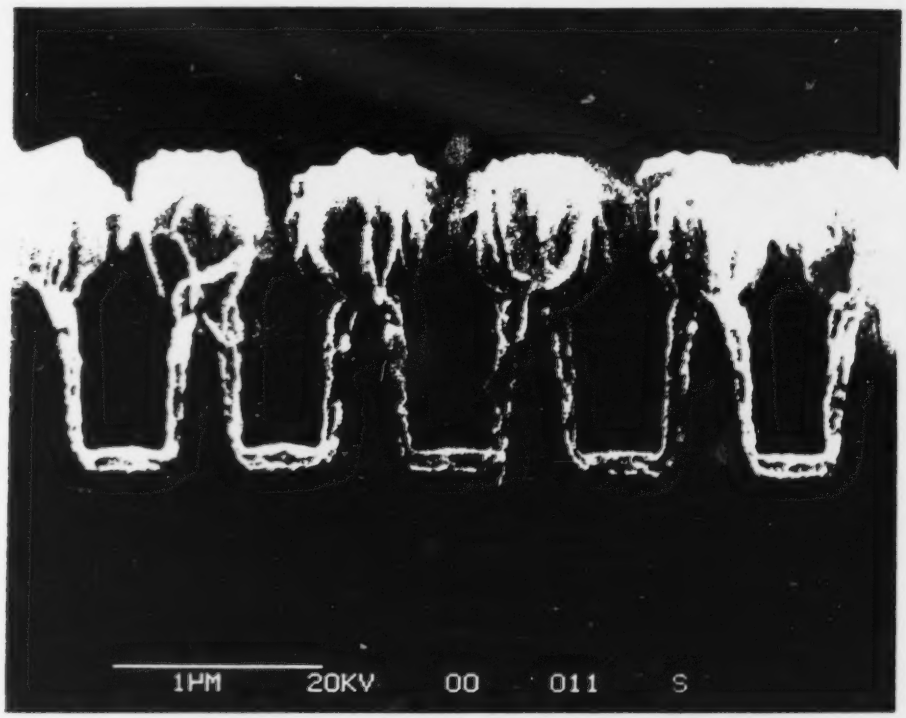

Figure 1.6 Conventionally sputter deposited aluminum on a series of oxide steps.

bottom and step coverages for the film shown in Figure 1.6 are 30 percent and 15 percent respectively, far from the ideal 100 percent.

The poor coverage on the trench is due to the shadowing effect of the oxide steps which prevent the sputtered flux from entering the trenches. As the aspect ratio of the trenches increases, the acceptance angle for sputtered flux to enter the trench is reduced correspondingly. The relationship of the flux acceptance angles at the bottom and the lower corner versus the width of a 1 μm deep trench is plotted in Figure 1.7. For trench widths of 1.5 μm or larger, the flux acceptance angles decrease slowly with the decreasing width. As the width drops below 1.5 μm, the flux acceptance angles fall linearly with the width. The abrupt drop of the flux acceptance angles for narrow trenches is the reason for the poor coverage of small features on today ULSI IC's.

Although the flux acceptance angle is almost the same at the corner and at the centre for a trench widths less than 1 μm, the bottom coverage on the micrograph shown in Figure 1.6 is much greater than the step coverage. The worse step coverage is caused by the additional shadowing from the portion of the film overhanging from the oxide step. This self-shadowing effect is more noticeable when the width of the trench is comparable or smaller than the overhang portion of the film.

Current minimum feature sizes of IC's have fallen below 0.5 μm, and 0.25 μm feature sizes are expected very soon [2]. Therefore, the filling of vias and trenches by sputtering is expected to deteriorate as the trend in feature size continues. As mentioned in Section 1.1.1, the inadequate filling on vias and trenches poses serious concerns

regarding electromigration. In addition to the reliability problem, the higher resistance at the thin areas will lower the operation speed of the circuits. The propagation delay due to RC time delay associated with an interconnect is given by [28]:

$$RC = \frac{\rho}{t_m}\frac{l^2 k}{t_{ox}} \tag{1.2}$$

where ρ and t_m are the resistivity and the thickness of the metal film, l is the length of the

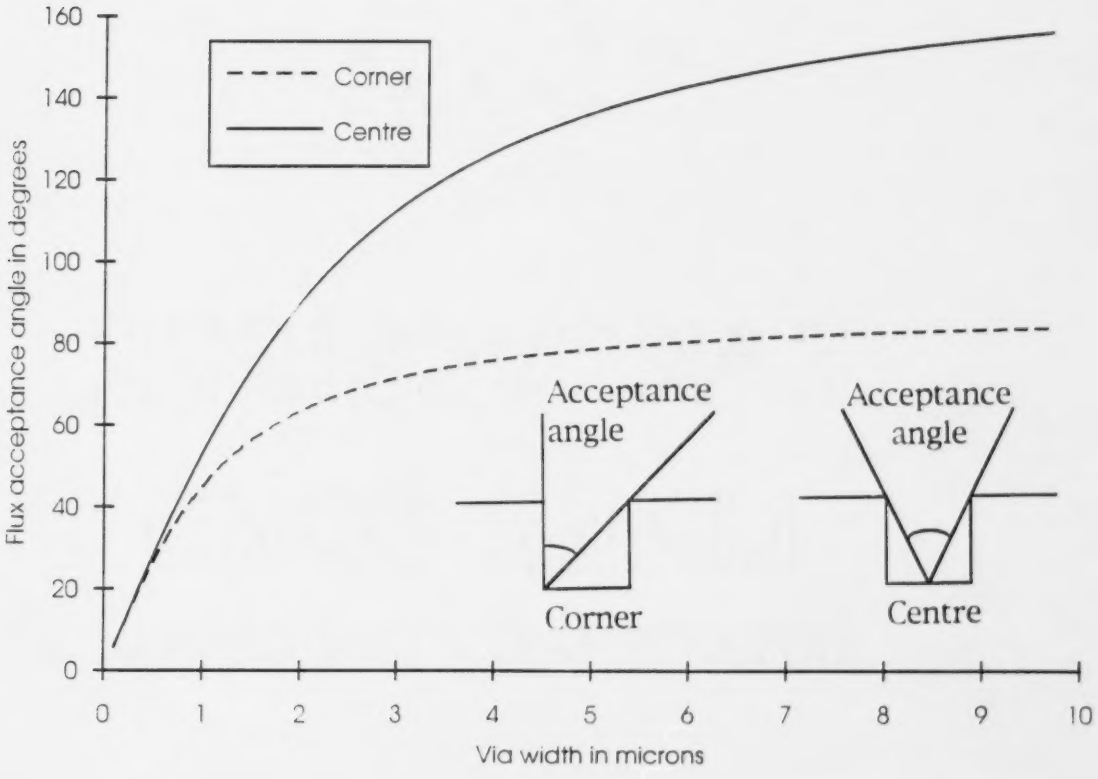

Figure 1.7 Flux acceptance angle at the corner and the centre of a trench as a function of the width of a 1 μm deep trench. The insert shows the definition of acceptance angle at the two locations.

interconnect, k is the dielectric constant of the oxide film, and t_{ox} is the thickness of the oxide films. The lower coverage on the side-wall and bottom of trenches increases the time delay and slows down the operation of the circuits.

Although the time delay can be reduced by increasing the thickness of the oxide film, a thicker oxide film would lead to higher aspect ratio features and consequently poor coverage. Therefore, the thicknesses of the oxide film has not been changed and remains at about 1 μm while the lateral dimensions of features on IC's continue to shrink.

In summary, conventional sputtering techniques are unable to provide sufficient coverage over small geometry in today's ULSI IC's. The poor coverage increases risk of electromigration and slows down the operation of IC circuitries. New metallization techniques are required for overcoming the deficiencies of conventional sputtering.

1.2 Emerging Techniques

In response to the needs for better coverage, new techniques are emerging to fulfill the metallization requirements. Bias sputtering [29, 30], tungsten plug [31, 32], laser irradiation [33, 34], and high temperature sputtering [35-37] are new techniques for combating the inadequate coverage provided by conventional sputtering. Each of these techniques has its own advantages and disadvantages, as described in the following sections.

1.2.1 Bias Sputtering

Bias sputtering is an effective technique for improving coverage. During sputtering, the substrate is biased to a negative electric potential so that the substrate is subjected to positive ion bombardment. The ions sputter off the film material accumulated at the top of vias and trenches, especially the overhang portion, and redeposit some of this material back into the vias and trenches. Although the biasing improves coverage, the bombardment by argon ions may introduce undesired side-effects. The incorporation of argon atoms and the growth of smaller grain films commonly associated with bias sputtering lower the electromigration resistance of the deposited film [30]. Also, the film is under compressive stress because of the ion bombardment during deposition. The reduced electromigration resistance and compressive stress currently limit the application of bias sputtering to ULSI metallization.

1.2.2 Laser Irradiation

The basic principle of aluminum reflow by laser irradiation is based on the ability of molten aluminum to drawn itself into vias and trenches due to surface tension. UV excimer laser is commonly used as the heat source for melting the aluminum [33 and 34]. The laser is pulsed at regular interval of several hundred Hz to irradiate the IC die during processing. The reasons for using UV laser are because of its ability on delivering short wavelength (easily absorbed by aluminum) and high energy density (up to several J/cm^2/pulse) light pulses[33 and 34] which is critical for melting aluminum at a very short time. The irradiated aluminum has very good electromigration resistance due to the large grain film resulted from the melting of aluminum. However, the difficulties with

maintaining a large area and uniform laser beam and maintenance problems with excimer laser have limited the use of the technique to research laboratories.

1.2.3 Tungsten Plugs

The conformal coverage poossible with chemical vapour deposited films make the tungsten plug process an attractive alternative to conventional metallization. Because of the high electrical resistance of tungsten, only the vias are plugged with tungsten and the rest of the interconnect is linked by lower resistance aluminum. The tungsten plugs can be fabricated by either blanket and selective depositions. For the blanket process, the substrate is completely covered by CVD tungsten The tungsten deposited on the dielectric is then removed by an etch-back process which leaves only the tungsten in the via. After the etch-back, the planarized surface is then covered with aluminum to complete the interconnect.

WF_6 is the precursor for the selective deposition process and does not dissociate easily on oxide or nitride surfaces to form tungsten [19]. Since the dielectric on IC's is either an oxide- or nitride-based material, tungsten is preferentially deposited on vias where the dielectric is etched out and the underlying metals or silicon are exposed. Thus, tungsten grows upward to form plugs. Although selective deposition is a simpler method, difficulties of controlling the selectivity have so far prevented large scale industrial application.

Although the coverage problem is resolved by using a tungsten plug, the electromigration resistance and the complexity of the process limit the usefulness of tungsten plug technology. Tungsten by itself is very robust to electromigration, but aluminum is depleted at the interface with tungsten without replenishment from the tungsten plug and consequently, and consequently open failure may result at the interface. A recent report indicated that the electromigration lifetime of aluminum metallization was superior than that of the combination of tungsten plug and aluminum metallization [38, 39]. The complexity of the process make tungsten plugs less attractive because of the added processing cost and the difficulty in attaining high yield. However, this process is currently in use.

1.2.4 High Temperature Sputtering

At a low deposition temperature, $T/T_m < 0.45$, the deposited materials remain close to their point of impact, and may cast a shadow on surrounding regions. To overcome this self-shadowing effect, the substrate can be heated to enhance the movement of material into vias and trenches of high concave curvature. Investigations have been reported of improved coverage by aluminum deposition at a substrate temperature between 500 and 550 °C [40, 41]. The virtues of this technique are the compatibility with the traditional metallization techniques and their simplicity for implementation. Only an additional substrate heating mechanism is required for implementation.

High temperature sputtering does have some disadvantages. Contamination due to outgassing from the chamber walls and the substrate heater during deposition would

adversely degrade the quality of the deposited aluminum film [42, 43], and the presence of impurity gases lowers the surface diffusion length of the aluminum adatoms [40, 44]. Thus, special care should be taken to ensure the cleanliness of the sputtering system. An ultra-high vacuum (UHV) environment is a necessity for high-temperature sputtered aluminum for ULSI metallization.

The reaction of aluminum with silicon at elevated temperatures can destroy the devices on IC's. To prevent the reaction, a metallic diffusion barrier is required to isolate aluminum from the silicon and maintain electrical continuity [45, 46]. Titanium nitride (TiN) is a commonly used barrier which is sufficiently effective at 550 °C [47].

Another concern with regard to high temperature aluminum is the possible adverse effect of heat on the dopant profile. Table 1.1 lists the bulk diffusion lengths of some common dopants in silicon after 1, 2, 3, and 4 hours of diffusion at 550 °C. The longest bulk diffusion length is 8.4×10^{-5} μm for aluminum, the fastest diffusing species. These diffusion lengths are much less than the dimensions of the doping profile on current IC's, therefore, dopant diffusion during deposition should not be a concern.

	Diffusion lengths in μm			
Dopant	1 hour	2 hour	3 hour	4 hour
P	1.0×10^{-5}	1.4×10^{-5}	1.8×10^{-5}	2.0×10^{-5}
As	4.4×10^{-6}	6.3×10^{-6}	7.7×10^{-6}	8.9×10^{-6}
B	1.6×10^{-6}	2.3×10^{-6}	2.8×10^{-6}	3.3×10^{-6}
Al	4.2×10^{-5}	5.9×10^{-5}	7.2×10^{-5}	8.4×10^{-5}

Table 1.1 Diffusion length of dopants in silicon at 550 °C.

High temperature sputtering has many advantages over other methods mentioned earlier, such as process simplicity, good electromigration resistance, and low electrical

resistance. However, the understanding of the relationship of film characteristics with deposition conditions is still limited. Thus, this thesis is in part devoted to the study of film properties and film growth parameters of high temperature sputtered aluminum.

1.3 Simulation

Simulation is an economic alternative to experimentation as the cost of equipment and processing is rapidly increasing. A simulation package, SIMBAD, was utilized for investigating the effect of deposition temperature (the dominant variable controlling diffusion) on the growth of aluminum films. The predictive power of SIMBAD has been verified for simulation of many IC fabrication-related thin film processes, such as sputtering, evaporation, CVD, reactive ion etching and plasma etching[27, 48-52], and has recently been extended to enable simulation of high temperature sputtering [53]. This thesis will be the first experimental verification of the ability of this new code to model specific films from an experimental system. Since the surface diffusion length of adatoms is very difficult to measure experimentally, the simulation will be a very useful tool for evaluating the effect of deposition temperatures on sputtered aluminum, and for estimating surface diffusion length.

Chapter 2 : Experimental Setup and Procedure

Due to the stringent vacuum and cleanliness requirements on the equipment for high temperature sputtered aluminum, an ultra-high vacuum (UHV) sputtering system was acquired for the experimental work in this thesis. The system was purchased from UHV Instruments Inc. which was responsible for the installation of the system, but the company went into receivership soon after system installation. Thus, full commissioning of the system became a part of this thesis work. The UHV system and the experimental procedure are described in this chapter.

2.1 System Requirements and Specifications

The diffusion and other properties of sputtered aluminum are very sensitive to residual gases in the deposition system, especially to oxygen and water vapour[18, 54, 55]. Verkerk reported that a partial pressure of water vapour at 5×10^{-6} Pa (3.8×10^{-8} Torr) [42] or oxygen at 2.5×10^{-6} Pa (1.9×10^{-8} Torr) [43] could adversely affect the properties of evaporated aluminum films. Rougher film surface, reduced grain size, weak <111> crystal orientation, and higher resistivity are the effects on aluminum films deposited at high concentrations of oxygen and water vapour. Both oxygen and water vapour are expected to have similar influences on sputtered aluminum films. To minimize the impact of residual gases, the deposition chamber base pressure must be kept below 2×10^{-8} Torr before sputtering.

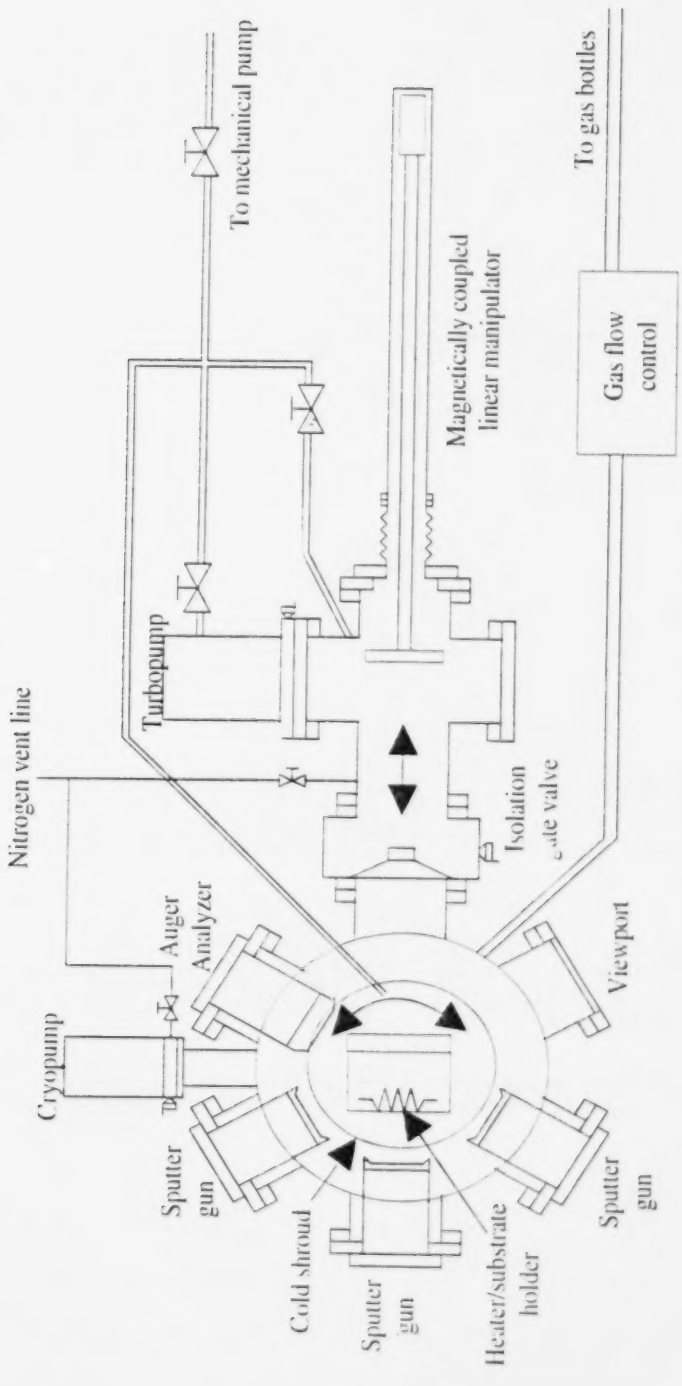

Figure 2.1 The schematic of the UHV sputtering system.

Baking the system prior to deposition and having a loadlock mechanism for sample transfer are indispensable for achieving this level of vacuum in a reasonable pump-down time. In addition to the above requirements, an additional pumping mechanism (cold trap) for water vapour is necessary for minimizing the effect of impurity gases during deposition. Table 2.1 lists the specifications of the sputtering system and Figure 2.1 shows the overall layout of the UHV sputtering system.

Table 2.1 Specifications and features of the UHV sputtering system.

1. Base pressure : in the low end of 10^{-9} Torr
2. Pump down time : less than 24 hours
3. Chamber side-wall bakeout capability
4. Loadlock
5. Sample transfer pressure : 1×10^{-7} Torr
6. Substrate heating : ≤ 600 °C
7. Cold trap for pumping water vapour

2.2 Setup of the UHV System

Three important features of the UHV sputtering system needed to achieve the cleanliness and temperature required for this process are the isolation of the main process chamber from atmosphere while loading and unloading samples, a substrate heating mechanism, and the cold shroud. These are discussed in detail in the following sections.

2.2.1 Loadlock

A loadlock arrangement was employed for isolating the main chamber from the atmosphere during sample loading and shortening the cycling time between depositions. The rough pumping for the loadlock was provided by a mechanical rotary pump made by

Edwards. An Edwards EXT250 turbomolecular pump (turbo-pump) was the high vacuum pump for the loadlock and the rotary pump also provided backing for the turbo-pump. Two vacuum valves, one at the loadlock and the other at the turbo-pump, switched the mechanical pump between the loadlock and the turbo-pump. The pressure in the loadlock was monitored by a Granville-Phillips 275 convectron gauge for pressure above 0.1 mTorr and a Granville-Phillips 274 nude Bayard-Alpert type ionization gauge for measurement below this pressure. The readouts of both pressure gauges were displayed on a Granville-Phillips 307 vacuum gauge controller. A manually operated gate valve was employed for isolating the chamber and loadlock. A magnetic-coupled linear manipulator was installed for transferring samples between the chamber and loadlock. A dry nitrogen line provided backfilling for the loadlock during loading and unloading samples. With the above arrangements, the loadlock was routinely pumped from atmospheric pressure to 10^{-7} Torr in 20 minutes.

2.2.2 Substrate Heating and Baking

Ohmic substrate heating was provided by a 2.5 m long by 0.5 mm diameter platinum coated molybdenum wire which was wound on the backside of the stainless steel heater/sample-hold assembly. The substrate temperature was monitored by a thermocouple on the heater/sample-holder assembly and was controlled by a Eurotherm 818 series temperature controller with a maximum output current of 10 A. The temperature controller had two modes of operation. The first mode was temperature feedback control. In this mode, the output from the thermocouple was fed back to the controller which automatically adjusted the output current to the heater wire to maintain

the temperature set by the operator. While the difference between the setpoint and feedback temperatures was greater than 30 °C, the controller delivered the maximum current of 10 A to the heater wire to achieve the minimum rise time on the substrate temperature. The temperature ramping from room temperature to 550 °C lasted more than 20 minutes.

The other mode of operation was manual control in which the heater current was set by the operator. In this mode, the operator must monitor the substrate temperature and adjust the heater current accordingly. Since the heating element was very stable and the thermal mass of the heater/sample-holder assembly was constant, the same heating current produced very similar substrate heat-up time from run to run. Typically, 8 A of the heater current would raise the substrate temperature from room temperature to 550°C in approximately 30 minutes. The manual mode could provide a longer operation life of the heater wire. However, all experiments in this thesis were performed with temperatures controlled in the feedback mode, before a better understanding of the temperature controller was attained.

A set of heat tapes and heat ribbons with total heating power of 1.2 kW were mounted on the outside surface of the chamber for baking the system before deposition. The heat tapes and heat ribbons were controlled by a Variac and a heat ribbon controller. A pair of thermocouples were mounted on the outside chamber wall for observation of the baking temperature. The chamber side-walls were never heated above 50 °C because of the presence of viton O-rings at several locations in the chamber. These O-rings could be damaged by prolonged heating at temperatures above 100 °C [56]. The substrate

heater was used for rising the temperature of the heater/substrate-holder assembly and substrate during baking.

2.2.3 Cold Shroud

Extra pumping of water vapour in the chamber was provided by a cold shroud which is made of steel. It is a hollow barrel surrounding the heater/substrate-holder assembly with openings facing sputter guns, view port, and loadlock gate valve. For activation, the cold shroud was chilled to -196°C (77 K) by filling it with liquid nitrogen. The pumping mechanism of the cold shroud was through adsorption of condensable gas species on the cold surface of the shroud. Since the cold shroud was situated inside the vacuum system and had a large pumping surface, the pumping speed was very high compared with conventional vacuum pumps. However, the pump capacity was limited. The pumping speed of the shroud was observed to decrease with time, due to saturation by pumped gas. Therefore, the cold shroud was activated only when the system was at a very low vacuum level and before deposition to preserve the pumping capacity for deposition.

2.2.4 Sputtering Chamber

The vacuum equipment on the main chamber consisted of a helium closed-cycle cryopump, a partial pressure analyzer (PPA) and three pressure gauges. The principal pump was a CVI 8-inch cryopump with pumping speeds of 1,700 L/s for nitrogen, 4,500L/s for water, and 1,400L/s for argon. Since the main chamber was not routinely exposed to the atmosphere except for the regeneration of the cryopump and maintenance,

no additional roughing arrangements were installed for it. In the case of pumping down from atmosphere pressure, the initial roughing was provided by the mechanical pump in the loadlock with the isolation gate valve opened. The turbo-pump acted as the second stage of roughing to further evacuate the chamber before the engagement of the cryopump, to minimize the gas loading.

The chamber pressure was monitored by three pressure gauges. The arrangement is similar to the loadlock with a convectron for pressure above 0.1 mTorr, a Bayard-Alpert type ionization gauge for pressure below 0.1 mTorr, and an additional Edward 127A capacitance manometer for monitoring pressure during sputtering. In addition to the pressure gauges, an Inficon Quadres partial pressure analyzer (PPA) was installed for leak checking. Since the PPA was mounted on the side of the main chamber through a section of 6" long tubing and a valve and no additional pumping was installed for it, the outgassing from the PPA housing became the dominant part of the measured partial pressure spectrum at low chamber pressure. Thus, the PPA was not used to analyze chamber gas composition. Instead, the PPA was a very sensitive leak detector when working with helium which is absent from the outgassing spectrum.

2.2.5 Basic Sputtering Equipment

A gas delivery system, three 2-inch magnetron sputtering guns, a DC magnetron power supply, and capacitance manometer comprised the core equipment for deposition. 99.9999 percent pure argon gas was delivered to the chamber through a Sierra 830 mass flow controller. The sputtering working pressure was monitored by an Edward 127A

capacitance manometer and displayed on the front panel of a VAT PM-5 adaptive pressure controller. The capacitance manometer had an operation range of 0.1 to 100 mTorr. The working pressure was controlled by the pressure controller through a VAT DN 63-320 stepper motor driven gate valve which was located between the cryopump throat and the chamber. The controller had two modes of operations, namely, adaptive feedback pressure control and manual control. When the controller was operated in the pressure feedback mode, due to the discrete nature of the stepper motor the gate valve was rapidly driven back and forth between steps even after pressure was stabilized. For a fixed gas flow rate, the same pressure could be obtained with only small adjustment by the operator on the gate valve position. Therefore, the pressure controller was only operated at the manual mode for all experiments.

Samples were mounted vertically on the heater/sample-holder assembly which was constructed on a rotating stage. The stage was differentially pumped by the mechanical pump to prevent leakage through the rotary seal on the stage. The heater/sample-holder assembly was located at the centre of the chamber with the cold shroud surrounding it. The samples could be rotated for access to each target on the chamber and to the loadlock.

2.2.6 Leak Checking and System Performance

After the installation, the system was leak-checked by the partial pressure analyzer, PPA, with helium. The leak check consisted of two stages; the chamber and the loadlock were checked and then the argon gas line was checked after ensuring no leaks

from the system. In the first stage, the PPA was operated in leak checking mode with the scanning mass set at 4 (helium atomic mass unit). Helium gas was sprayed at all fittings and joints on the chamber and loadlock. After thorough checking, no leaks were detected on the chamber.

After the confirmation of no leaks to the chamber, the gas line for delivering argon gas to the chamber was checked. The mass flow controller that linked the gas line to the chamber was set to maximum flow with gas tank valve closed so that the gas line was evacuated and could be leak-checked with the PPA. During the leak checking, some fittings were found to be leaky. All leaks were repaired by replacing these fittings.

After the leak checking, the ultimate base pressure achieved by the cryopump with the substrate heater and heat tapes shut off was 7×10^{-10} Torr after a day of baking on the chamber side-walls. With the cold shroud, the base pressure could reach as low as 3×10^{-10} Torr. The performance of the UHV system was satisfactory in terms of short pump down time and low base pressure.

2.3 Estimation of Background Gas Pressure during Deposition

As noted earlier, the level of oxygen and water vapour partial pressure during sputtering has detrimental effects on the mobility of adatoms and film properties of sputtered aluminum. A knowledge of the oxygen and water vapour partial pressure would be helpful for assessing the cleanliness of the UHV system. The base pressure before deposition is commonly used for evaluating the presence of background gases, but the different pumping arrangement during deposition will lead to an impurity partial

pressure different than that of the base pressure. An estimation of the impurity partial pressure during deposition is presented in this section.

During deposition, the sources of gaseous impurities are the impurities in the working gas, and outgassing from the chamber wall. UHP grade 99.9999% pure argon gas was employed in the experiments to minimize the first source of impurities. The outgassing was minimized through use of the cold shroud and by pre-deposition baking. The impurity partial pressure, P_{ig}, from the argon working gas is :

$$\begin{aligned} P_{ig} &= P_w * (1 - \text{purity of argon}) \\ &= 10 \times 10^{-3} \times (1 - 0.999999) = 1.0 \times 10^{-8} \text{ Torr} \end{aligned} \tag{2.1}$$

where P_w is the working pressure which had a maximum value of 10 mTorr. This level of partial pressure is at the upper limit for deposition of high quality aluminum at high temperature[42]. The contribution from the outgassing must be small enough to keep the partial pressure below 2×10^{-8} Torr.

The calculation for outgassing is more complicated than P_{ig} and some assumptions are made. The majority of outgassing is assumed to occur from the heated substrate and the heater/substrate-holder assembly because outgassing is a thermally activated process [56, 57] which increases with temperature. Since water vapour is the major component released from a heated surface [57], a conservative estimate (i.e. worst case) is made with the assumption of water vapour being the only constituent of outgassing. Accounting for the worst case situation, the substrate is assumed to be heated to 550 °C which is the highest substrate temperature used in this work. Also, the system is assumed to be at thermal equilibrium, i.e., no sudden change of temperature. The last assumption is not

true for the 3-step deposition experiment which involves ramping up the substrate temperature during deposition, but it is used to simplify the calculation.

The outgassing rate, Q_{out}, of the system before deposition is the product of its base pressure, P_{base}, and the total pumping speed, S_{sys} (See Eq. 2.2), of the system. Q_{out} is 4.5×10^{-6} Torr•L/s for a typical P_{base} at 1×10^{-9} Torr with the substrate temperature at 550 °C and S_{sys} of H_2O at 4,500 L/s.

$$Q_{out} = P_{base} * S_{sys} \tag{2.2}$$

The partial pressure, P_{out}, of outgassing species during sputtering is the outgassing rate divided by the pumping speed, S_w, during the deposition. Since the pump throat is throttled for regulating the working pressure, S_w is less than S_{sys}. S_w is calculated by a similar expression for Q_{out} and is shown below:

$$S_w = \frac{Q_w}{P_w} \tag{2.3}$$

With the working gas flow rate, Q_w, of 15 standard cubic centimeters per minute (sccm) of argon and the working pressure, P_w, of 10 mTorr, the pumping speed of the throttled cryopump is 19 L/s which is less than 1 percent of S_{sys} for Ar. The corresponding throttled pumping speed for water is 61 L/s. The partial pressure, P_{out} of impurities due to outgassing during deposition is given by:

$$P_{out} = \frac{Q_{out}}{S_w} = \frac{4.5\times10^{-6}\ \text{Torr}*\text{L/s}}{61\ \text{L/s}} = 8\times10^{-8}\ \text{Torr} \tag{2.4}$$

This level of water vapour partial pressure is too high for depositing high quality

aluminum film, especially at high substrate temperature. Since P_{out} is much larger than P_{ig}, outgassing is the dominant source of impurities.

The above calculation does not include the additional pumping speed provided by the cold shroud. The cold shroud has a limited pumping capacity which is easily saturated by the injection of argon gas. However, the pumping speed for water vapour, which is assumed to be the only component of the outgassing, is still high due to the small outgassing rate of the water vapour. The pumping speed of the cold shroud is estimated by comparing the base pressure obtained by the cryopump and by the cold shroud independently under a single pumping session. Since the outgassing rate for both situations are the same (assume the shroud is not the dominated source of outgassing), the relationship between the pumping speed of the cryopump and the cold shroud can be expressed as:

$$Q_{out} = P_{cryo}S_{cryo} = P_{cold}S_{cold} \tag{2.5a}$$

$$S_{cold} = \frac{P_{cryo}}{P_{cold}} S_{cryo} \tag{2.5b}$$

where P and S are the base pressure and pumping speed, respectively and with the subscripts cryo and cold denoting the pumping mechanism of the cryopump and cold shroud. The measured P_{cryo} and P_{cold} were 1×10^{-9} Torr and 3×10^{-10} Torr, respectively. With the pumping speed of water for the cryopump at 4500 L/s and the assumption of water vapour as the only constituent of outgassing, the pumping speed of the cold shroud is 15,000 L/s. With this pumping speed, P_{out} is 3×10^{-10} Torr.

The contamination by water vapour can be further reduced by depositing films at high rate so that the deposition rate is much higher than the impingement rate of water vapour molecules on the sputtered film. For the 1-step method, the deposition rate was approximately 6×10^{16} Al atoms per cm^2 per second based on the deposition rate of 0.13 μm per minute. The impingement rate (Γ) for 3×10^{-10} Torr of water vapour pressure can be calculated by [57]:

$$\Gamma = P\sqrt{\frac{1}{2\pi m k_B T}} \tag{2.6}$$

where P and m are the pressure and the molecular mass of water and k_BT is thermal energy. Γ was found to be 9×10^{10} water molecules per cm^2 per second. The resulting concentration of water molecules is approximately at one part in 5×10^5.

2.4 Deposition Procedures

The effect of substrate temperature on sputtered aluminum in two deposition processes was investigated in this thesis. The experimental procedures for the 1-step deposition experiment and 3-step process are described in Sections 2.4.2 and 2.4.3, respectively. The substrates and their preparation are described in Section 2.4.1.

2.4.1 Substrates and Their Preparation

Two types of substrates were used for the experiments. The first type was used for examining the film stress and sticking coefficient of the deposited aluminum film. An in-house fabricated overhang structure was used for these purposes, and is shown in cross-section in Figure 2.2. The overhanging layer is thermal oxide which was patterned

with standard lithography processes utilizing buffered-oxide-etch. The overhang is released from the silicon underlay by an etching solution which is composed of 2 % HF: 95 % HNO_3 : 3 % acetic acid by volume. The required etch time for the sample shown in Figure 2.2 was 6 minutes.

The other type of substrate is a Northern Telecom processing test die (NT die). The die is covered with a layer of SiO_2 and has many test via holes and trenches on it. The filling profile, grain size, and crystal orientation of aluminum films were studied with this die.

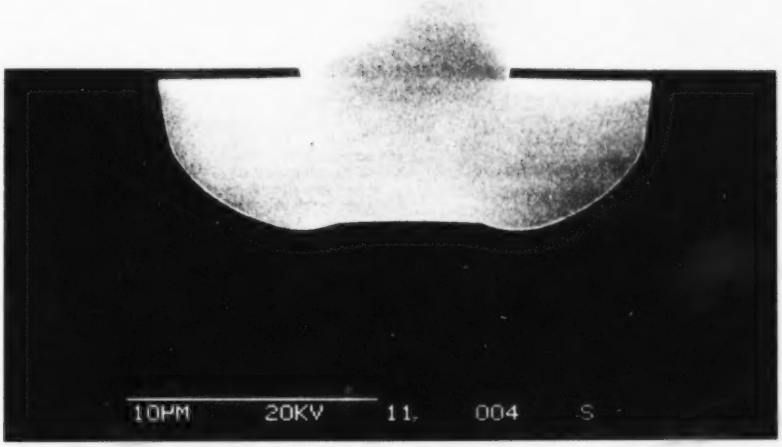

Figure 2.2 Cross-sectional view of an overhang structure.

All substrates were individually cleaned with isopropyl alcohol in an ultrasonic cleaner for 5 minutes, followed by 3 washes with deionized water in the ultrasonic

cleaner for 5 minutes per wash. The samples were blown dry with dry nitrogen gas. After cleaning, the samples were placed in the loadlock and kept under vacuum for outgassing and protection from contamination before usage.

2.4.2 Baking and Sample Loading

The main chamber side-walls were heated to approximately 30 °C prior to and during the loading of a sample. The sample was first mounted on a sample holder and then loaded onto the magnetically-coupled linear manipulator in the loadlock. The loadlock was then pumped down by the roughing pump and then by the turbo-pump. In approximately 20 minutes after the engagement of the turbo-pump, the pressure in the loadlock would drop down to 1×10^{-7} Torr, at which point the sample was transferred to the main chamber using the linear manipulator arm. The isolation gate valve was opened only during the transfer process.

To minimize outgassing from the chamber side-wall and the heater/substrate-holder assembly during the deposition, the chamber was baked at 30 °C for 5 hours before each deposition. After the sample was loaded, the substrate temperature was set to 600 °C, which was 50 °C above the highest deposition temperature, so that the amount of outgassing could be maximized during baking. The heat tapes were turned off and the substrate temperature was set to deposition temperature before the end of a day so that the chamber would cool down to room temperature and the substrate would settle to the deposition temperature by the next morning. The minimum baking time used for the chamber was 5 hours.

The following morning, the substrate temperature was stabilized at the predetermined setting and the chamber side-wall was cooled down to room temperature. The ion gauge in the chamber would indicate a vacuum level typically 1×10^{-9} Torr or lower, depending on the substrate temperature. At this point the system was ready for deposition.

2.4.3 1-step Deposition Experiments

Three substrate temperatures, 550 °C, 300 °C, and room temperature, were chosen for studying the effect of substrate temperature on the properties of the sputtered aluminum films. The room temperature case was used as an reference for comparison with the elevated temperature cases and the 300 °C case was selected as an intermediate point. 550 °C is the typical temperature for the hot aluminum deposition process reported by others [18, 30, 58]. For the room temperature case, the substrates were not heated during deposition, but the film surface temperatures were expected to rise above room temperature during deposition. The heating up of the film surface is caused by the kinetic energy carried by the sputtered atoms, which ranges from few eV to tens of eV and by energetic reflected neutrals [21]. The deposition process without substrate heating is denoted as RT and consequences of "self-heating" will be discussed further in Chapter 4. The other deposition parameters for this set of experiments were 6 minutes deposition time, 300 W sputtering power, 15 sccm argon gas flow rate, and 10 mTorr pressure. The deposition sequence is described in the following paragraphs.

Before sputtering, the cold shroud was activated by filling it with liquid nitrogen. Argon gas was admitted into the deposition chamber at a flow rate of 15 sccm and then the gate valve between the chamber and the cryo-pump was partially closed to lower the effective pumping speed for regulation of the working argon pressure. The working pressure was monitored by the capacitance manometer and the readout of the capacitance manometer was displayed on the pressure controller front panel. The gate valve position was adjusted manually through the pressure controller until the desired pressure was achieved.

After the pressure and gas flow were stabilized, a plasma was ignited by a MDX 1K DC magnetron power supply made by Advanced Energy Industries Inc. The target was conditioned by a pre-deposition sputter clean for at least 1 minute before opening the target shutter for the actual deposition. The deposition was carried out at 300W sputtering power for 6 minutes. After the film was deposited, the plasma was turned off immediately. Also, the gas flow was zeroed, the cryopump gate valve was opened completely to evacuate the system, and the substrate heater was turn off. Finally the sample was transferred back to the loadlock which was vented with nitrogen to atmosphere pressure before unloading. The experimental sequence of this type of experiment is summarized in Table 2.2.

2.4.4 3-step Deposition Experiment

The initial stages of film growth are discontinuous and clustered. At high deposition temperatures, these film nuclei tend to grow larger and farther apart on the substrate due in part to longer surface diffusion lengths. Figure 2.3 is a sketch

Table 2.2 1-step deposition procedures

1. Turn on the chamber heat tape to warm up the chamber to approximately 30 °C.
2. Mount a sample on a sample holder.
3. Pressurize loadlock with dry nitrogen and load sample onto the linear manipulator arm.
4. Close-off loadlock door and nitrogen flow and rough out with the rotary pump to 1 Torr by opening the roughing valve .
5. Shut off roughing valve and open backing valve for turbo pump.
6. Engage turbo pump.
7. Open isolation gate valve after loadlock pressure drops to 10^{-7} Torr.
8. Transfer sample to heater/sample-holder assembly by sliding and tilting the linear manipulator arm.
9. Retract linear manipulator arm and close-off isolation gate valve.
10. Set substrate temperature to 600 °C at the substrate heater controller.
11. After 5 hours, shut off chamber heat tape and lower the setting on the substrate heater controller to deposition temperature. (Note : no substrate heating for RT case.)
12. The next morning, the substrate temperature should be stabilized at the deposition temperature and the chamber temperature should settle to room temperature.
13. Activate the cold shroud by filling it with liquid nitrogen.
14. Inject 15 sccm argon gas into the chamber.
15. Adjust cryopump gate valve to set the chamber pressure to 10 mTorr.
16. Start plasma with 300 W sputtering power.
17. Let target be sputtered clean for at least one minute before opening the target shutter.
18. Open target shutter to start the deposition.
19. After 6 minutes sputtering, close off target shutter and turn off plasma.
20. Shut off argon, open throttle on cryopump and transfer sample to loadlock.
21. Unload sample.

representative of the initial film growth of aluminum deposited at 550 °C. When the large nuclei grow at the top of a trench or via, the nuclei intercept vapour flux entering the trench or via. Consequently, the nuclei continues to expand and block more flux. This phenomena is schematically illustrated in Figure 2.3b. A 3-step deposition method (see Figure 2.3a) was reported to counteract the poor coverage due to the uneven wetting on the substrate [44, 59]. At the initial stage, aluminum is deposited at room temperature to form a complete wetting layer of aluminum on the substrate. After forming the wetting layer, the substrate temperature is ramped to 550 °C. During the temperature ramping, deposition continues at a slow rate to prevent oxidation on the freshly deposited film. After the substrate temperature reaches 550 °C, the sputtering resumes at the high rate to complete the deposition.

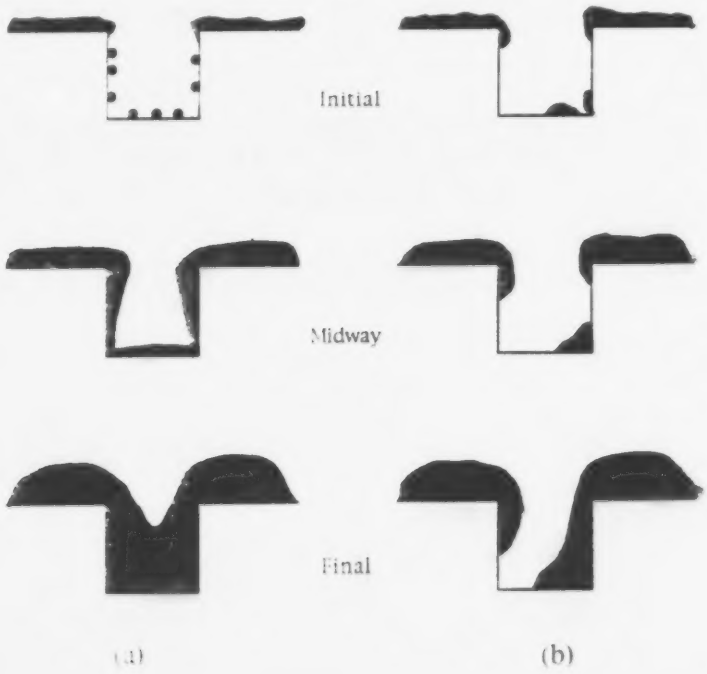

Figure 2.3 The film growth sequence of a) 3-step and b) 1-step deposited hot aluminum films [44]

For the 3-step experiment, the sample cleaning, loading, baking, and target pre-cleaning procedures were the same as the 1-step temperature effect experiment. A different deposition sequence was used for the 3-step experiment. After the target pre-clean, the deposition proceeded at room temperature for 5 minutes with a sputtering current of 500 mA which provided a deposition rate of approximately 70 nm/min. At the completion of the first layer, the substrate temperature setting on the heater controller was changed from 0 °C (no heating) to 550 °C and the sputtering current is lowered to 100 mA. The corresponding deposition rate was approximately 13 nm/min. The substrate required approximately 20 minutes for its temperature to rise to 550 °C. After the temperature was stabilized at 550 °C, the sputtering current was reset to 500 mA for another 5 minutes of sputtering to finish the deposition. The deposition sequence of 3-step experiment is outlined in Table 2.3.

Table 2.3 3-step deposition sputtering parameters.

Step	Substrate heating	Sputtering parameters		
		Time	Current	Pressure
1	No heating	5 minutes	500 mA	10 mTorr
2	Ramping up	20 minutes	100 mA	10 mTorr
3	Maintained at 550 °C	5 minutes	500 mA	10 mTorr

Chapter 3 : Experimental results

After many films were deposited, the deposition processes were refined as described in Section 2.4. The films analyzed in detail here are representative of the best results obtained. The 1-step deposited films were characterized by their coverage over trenches, surface curvature, grain size, stress, and crystal orientation. This work is discussed in Section 3.1. The results from the 3-step process are compared with the 1-step 550 °C deposited film in Section 3.2. The coverage over trenches and vias for the 1-step 550 °C films and 3-step films are discussed in Section 3.3.

3.1 1-step Deposition Process

The coverage, stress, grain size, and crystal orientation of the aluminum films sputtered at the three studied temperatures are reported in this section. The film coverage was examined by SEM on fractured cross-sections of the NT die. The grain size was evaluated from the top views of film deposited on planar areas of the NT die. The crystal orientation was examined by x-ray diffraction (XRD). The film stress was examined and calculated from the bending of overhang structures.

3.1.1 Coverage

The SEM micrographs of aluminum films deposited over trenches at the three substrate temperatures, namely, RT, 300 °C and 550 °C, are shown in Figure 3.1. For films deposited at RT, the aluminum extended over the edge of the oxide walls and blocked the sputtered flux from entering the bottom of the trench. The accumulation of

aluminum on the top of the trenches can be explained by the low mobility of the adatoms during deposition. The deposited atoms do not diffuse far from their impact sites and thus, shield the neighbouring area from the incoming sputtered flux. This effect is most pronounced along the side-walls and bottom corners of the trench where the least amount of material was deposited. Another distinct feature of the RT films is a small hump of aluminum at the centre of the trenches. The thicker coverage is created by a relatively larger flux acceptance angle at the centre than at the corners; thus, more material was deposited at the centre. It was noted that the surface of the RT film is the roughest among the three shown in Figure 3-1.

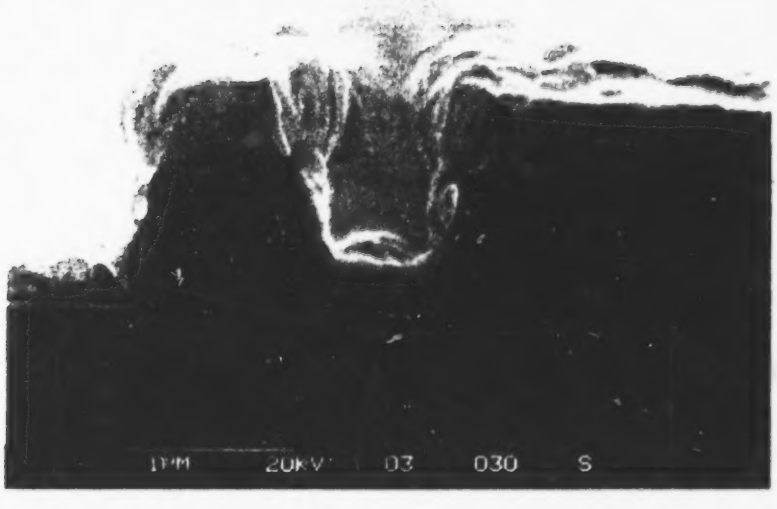

Figure 3.1a Trenches 0.75 μm wide by 0.85 μm deep are shown covered with aluminum sputtered at RT.

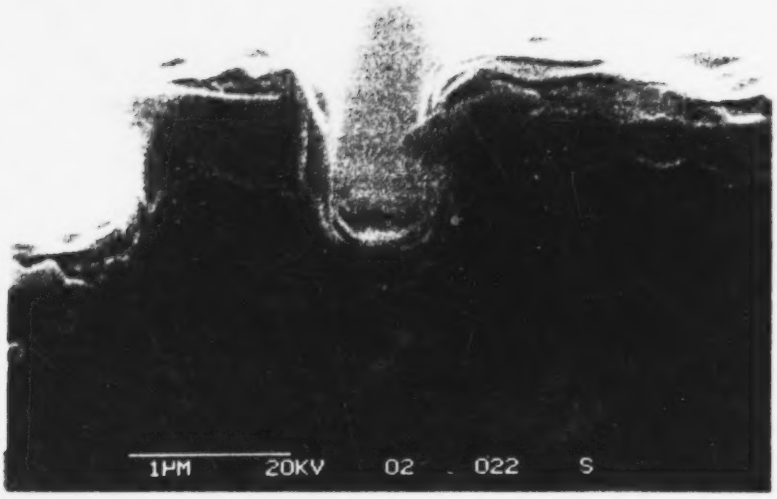

(b)

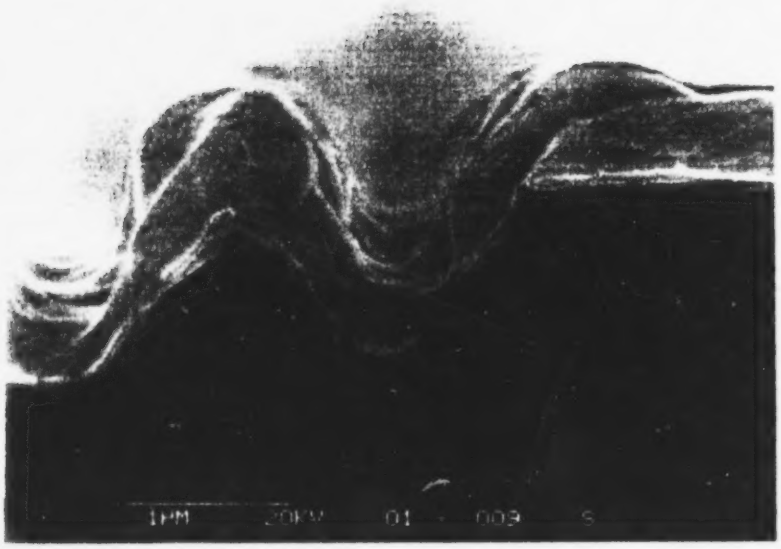

(c)

Figure 3.1 Trenches 0.75 μm wide by 0.85 μm deep are shown covered with aluminum sputtered at a) RT, b) 300 °C, and c) 550 °C.

The surfaces of films deposited at 300 °C are smoother and rounder than the RT films. The overhang feature at the top of the trench and the hump at the centre of trench on the RT films are not seen on the 300 °C film. The disappearance of these features is caused by the increase of adatom mobility. With less self-shadowing, the bottom coverage is reasonable at 70 % and is approximately 55 % better than the RT case. The film profile resembles the original rectangular trench, but with a narrower opening. Consequently, a higher aspect ratio trench resulted from the deposition. The dimensions of the new trench are 0.5 μm wide by 1.2 μm deep, and so the new aspect ratio is 2.4, whereas the original aspect ratio was 1. With this higher aspect ratio, the amount of sputtered flux entering the trench is expected to be reduced as deposition continues.

For the 550 °C case, the film profiles are well rounded and the surface is smooth. Due to the tapered side-walls of the aluminum film, the shadowing effect of the side-walls is reduced and the coverage is expected to improve as the deposition continues. The coverages of the 550 °C films are the best among the three films, with the results for all films shown in Table 3.1.

Table 3.1 Side-wall and bottom coverage on trenches

	Substrate temperature		
Coverage	RT	300 °C	550 °C
Side-wall	14 %	23 %	100 %
Bottom	45 %	70 %	100 %

Both the bottom coverage and side-wall coverage improve with increasing deposition temperature. The very poor side-wall coverage for the lower temperature

cases is created by the non-uniform density of sputtered flux and by the low adatom mobility. The angular distribution of the flux is symmetric and more concentrated about the normal to the wafer and thus, the side-walls receive at most only half of the incident flux with the other half being blocked by the side-wall itself. Self-shadowing by the film deposited at the top of the trench further reduces the flux (especially the normal incident flux) from hitting the side-walls. The self-shadowing is most noticeable at the area just below the overhang in the RT film. Similar arguments explain why the trench centre, which is open to flux arriving at near-normal incidence, has a better coverage compared to the side-walls.

In summary, both the bottom and side-wall coverages on trenches improved with an increase of the deposition temperature. This improvement is a result of the longer surface diffusion length which allows sputtered atoms to diffuse into the trenches. At low deposition temperatures, the shadowing effect limited the coverages. Note also that the film curvatures at the corners of the trenches are reduced at higher deposition temperatures. The topic of surface curvature and its importance in diffusion is discussed in the next section.

3.1.2 Surface Curvature

The additional thermal energy on a heated substrate allows adatoms to diffuse for a longer distance before being incorporated into the bulk of the film. On average, the mobile adatom will find a site that results in a minimization of surface energy (or potential energy) as shown in Figure 3.2.

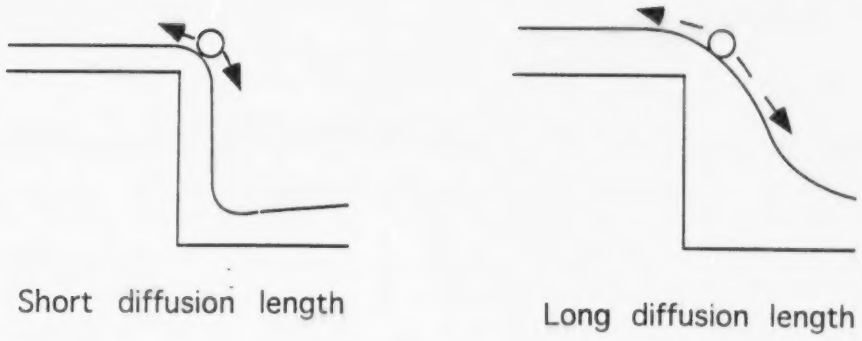

Figure 3.2 The relationship between adatom surface diffusion length and film surface curvature.

Thus, the radius of surface curvature of the films should be larger at the elevated substrate temperatures. This is indeed the case for the films shown in Figure 3.1. The radii of curvature of films at 3 temperatures were measured at both the convex corners at the top of the trenches and concave corners at the bottom of the trenches. These results are shown graphically in Figure 3.3.

For the room temperature and 300 °C cases, the radius of curvature is smaller at the concave corners (negative curvature) than at the convex corners (positive curvature). This can be explained by the shadowing effect and low adatom mobility. Before adatoms are incorporated into a film, they will diffuse over the surface a distance which is determined on average by the substrate temperature. The majority of the flux deposited on the trenches impact on the top half of the trench side-walls due to shadowing of the

lower features. As the curvatures at the top corners are decreased by the mobile adatoms (note, curvature is the reciprocal of radius of curvature), some aluminum atoms are ultimately deposited at the middle of the side-wall. These side-wall deposits will increase the curvature at the lower concave corner. For the 550 °C case, the diffusion length was of the order of the substrate feature size so that adatoms impacting at the top of the trench were able to diffuse into the bottom of the trench. Also, the opening of the trench in the 550 °C film allowed more flux to enter the bottom of the trench. Why the radius of curvature on both the concave and the convex corners of the 550 °C film are the same is

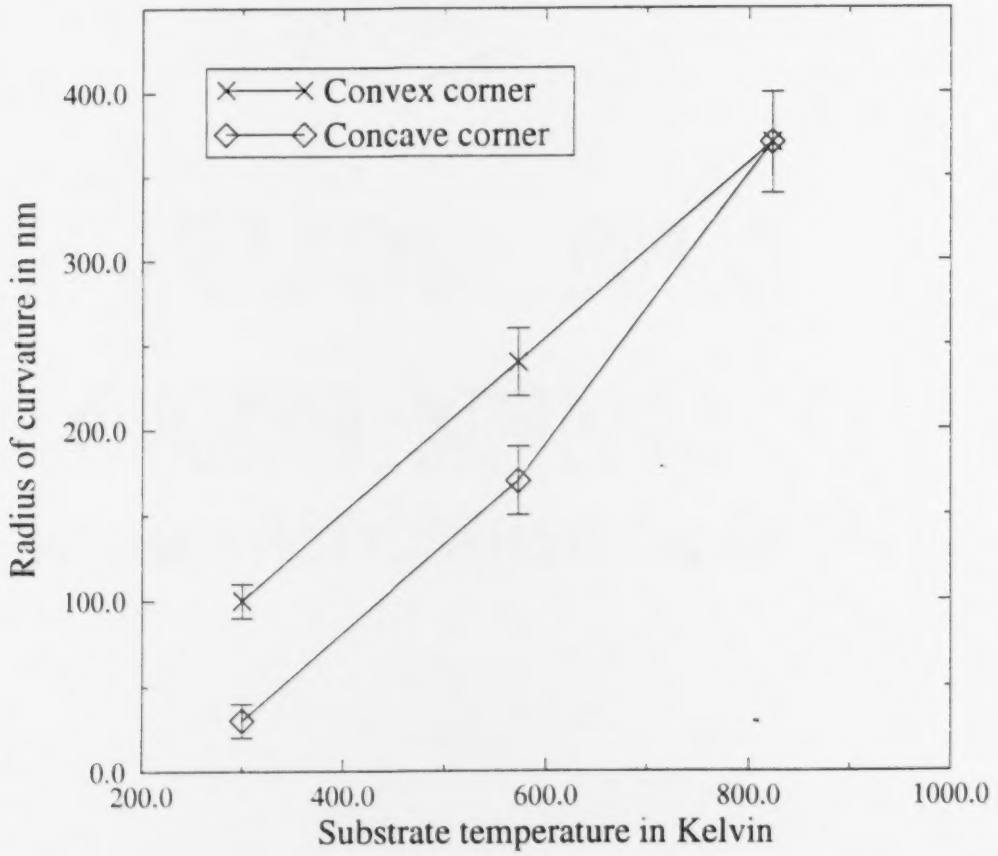

Figure 3.3 Radius of curvature of aluminum films sputtered at different deposition temperatures.

3.1.3 Grain Size

Annealing is a common post-deposition process to increase grain size and release crystallographic defects in sputtered films and form ohmic contacts to silicon. Annealing for aluminum is typically conducted at temperatures between 300 °C and 450 °C [61]. As the deposition temperatures of the films studied approaches or exceeds the annealing temperature for aluminum, the grain size and crystal quality of the resulting films should vary with the depositing temperatures.

Figure 3.4 shows the top views of the films of Figure 3.1 and shows clearly a grain size increase with deposition temperature. The standard method for determining grain size for bulk samples is to measure the grain density on a cross-section of the samples and use the relationship of Eq. 3.1 to determine the grain size [62]:

$$\log(d) = -0.4 - 0.05\log(n) \tag{3.1}$$

where d is the average grain diameter and n is the number of grains per mm^2 when viewed on a ×100 magnification. For thin films, the top surface is a reasonable representation of a cross-section in the plane of the film. The measured grain sizes are plotted in Figure 3.5.

The trend of increasing grain size with higher substrate temperature corresponds with predictions of the structure zone model. The larger grain size of high temperature deposited aluminum suggests that the electromigration resistance for these films is improved by the higher substrate temperature. Crystal orientation will also affect electromigration resistance and is the topic of the next section.

(a)

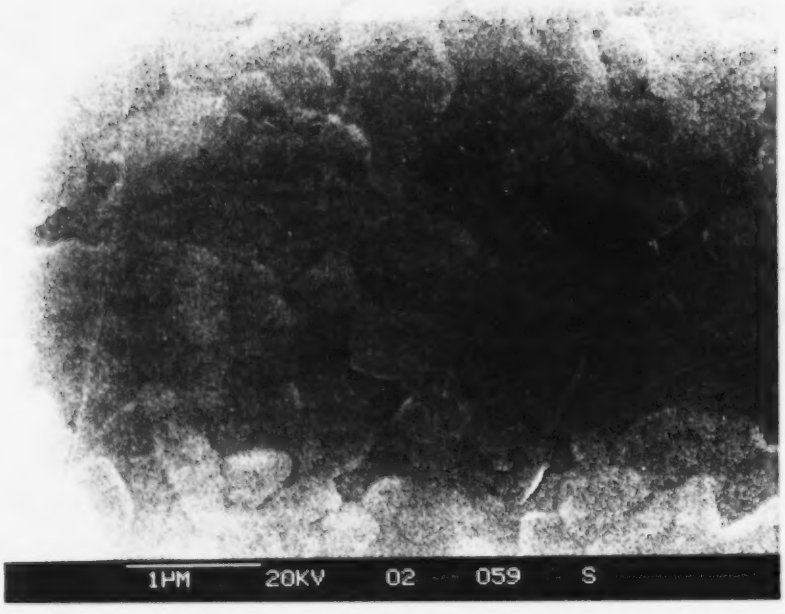

(b)

(figure continued ...)

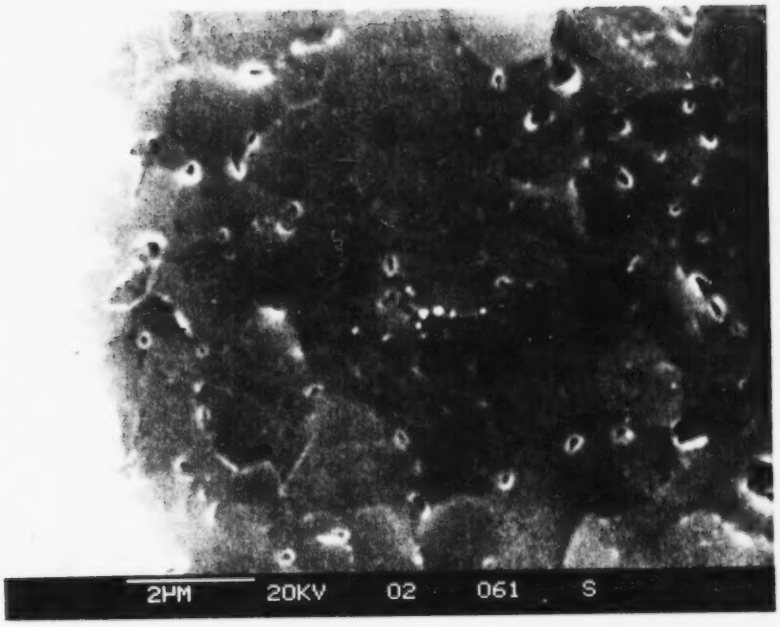

(c)

Figure 3.4 Top views of the aluminum films sputtered at a) room temperature, b) 300 °C, and c) 550 °C. Note that the scale bar varies for each SEM photograph.

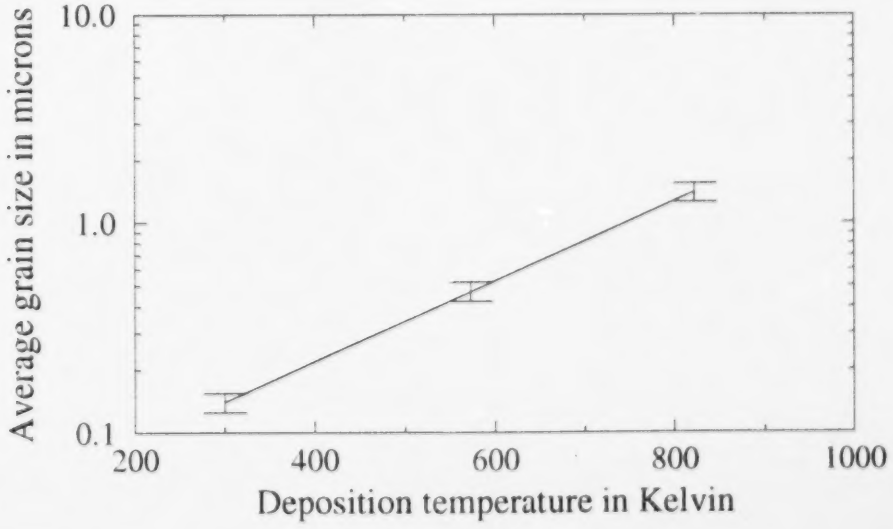

Figure 3.5 Aluminum grain size increases with substrate temperature.

3.1.4 Crystal Orientation

The crystal orientation of aluminum films is an important factor in determining the electromigration resistance of the film. As discussed earlier, a strongly <111> oriented aluminum film has a longer MTF than a <200> oriented film. The XRD analysis of RT film is shown in Figure 3.6. The large peak at the extreme right of Figure 3.6 is from the silicon substrate and the two centre peaks are from the deposited aluminum. To show more details near the aluminum peaks, Figure 3.7 gives enlarged views of the scans for $30° < 2\theta < 70°$ for the three studied films.

Table 3.2 Identification of XRD peaks with ASTM x-ray powder files

	Powder Interplanar Spacing (Å)	Measured Interplanar Spacing (Å)		
		550 °C (823 K)	300 °C (573 K)	RT (300 K)
Au <111>	2.355	-	-	2.357
Al <111>	2.338	2.333	2.330	2.335
Au <200>	2.039	-	-	2.036
Al <200>	2.024	-	-	2.020

Individual peaks from each scan in Figure 3.7 are listed and identified in Table 3.2 through comparison with ASTM x-ray powder files. The gold peaks in the RT film originated from the gold coating on the sample, used for contrast enhancement in SEM studies.

The <200> peak is observed only on the RT deposited sample and is very small. The ratio of the intensities of <111>/<200>, which is a common quantity for evaluating the crystal quality of aluminum film, is 7. This strong <111> and weak <200> orientation

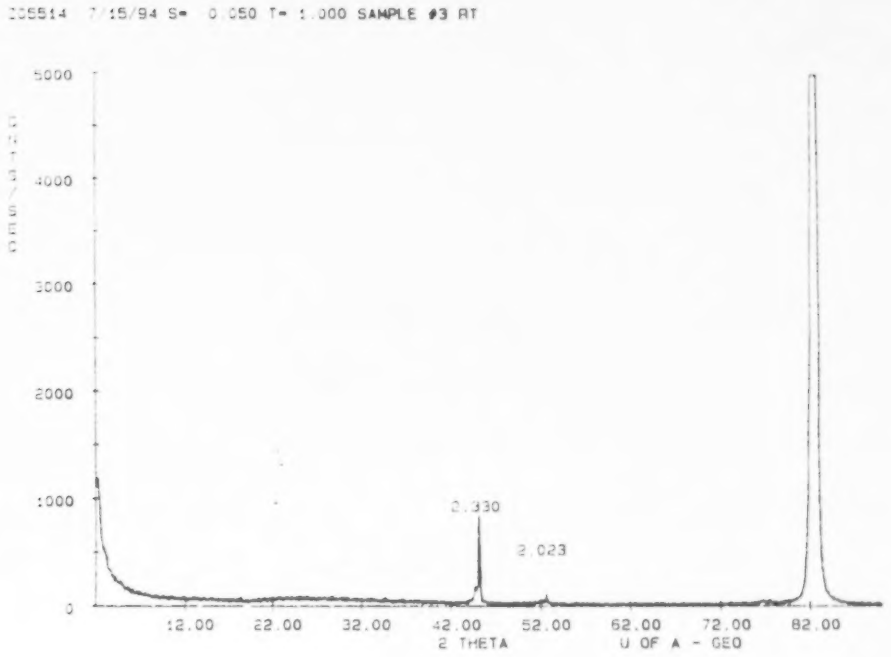

Figure 3.6 XRD scan of aluminum film sputtered at room temperature.

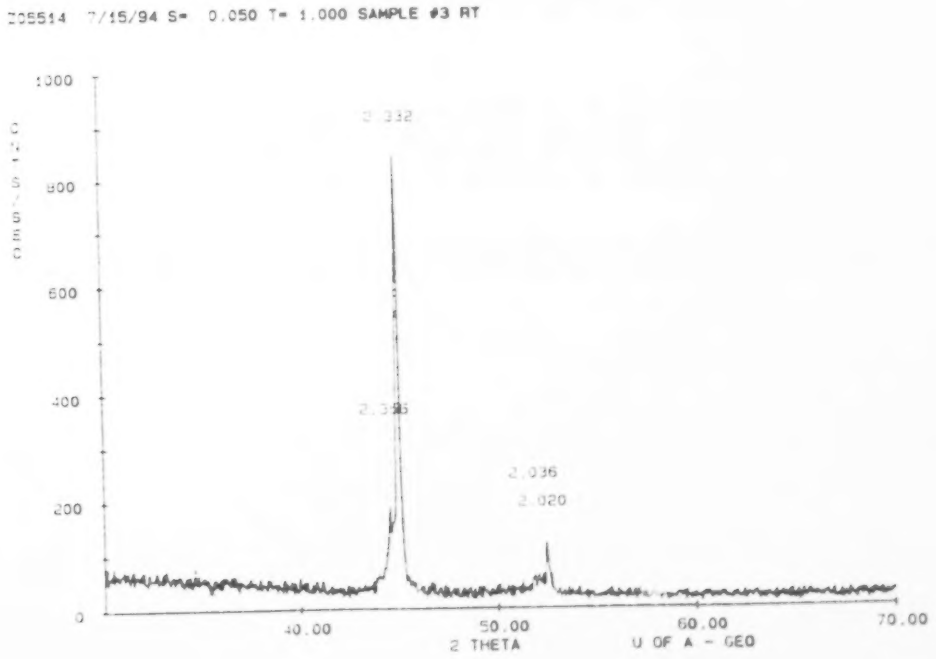

(a)

(figure continued ...)

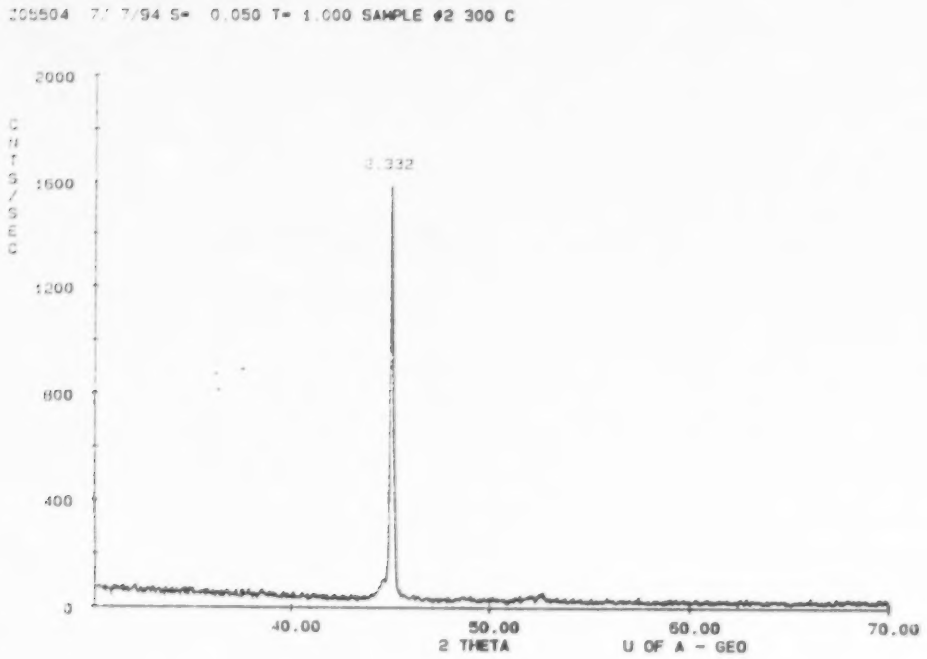

(b)

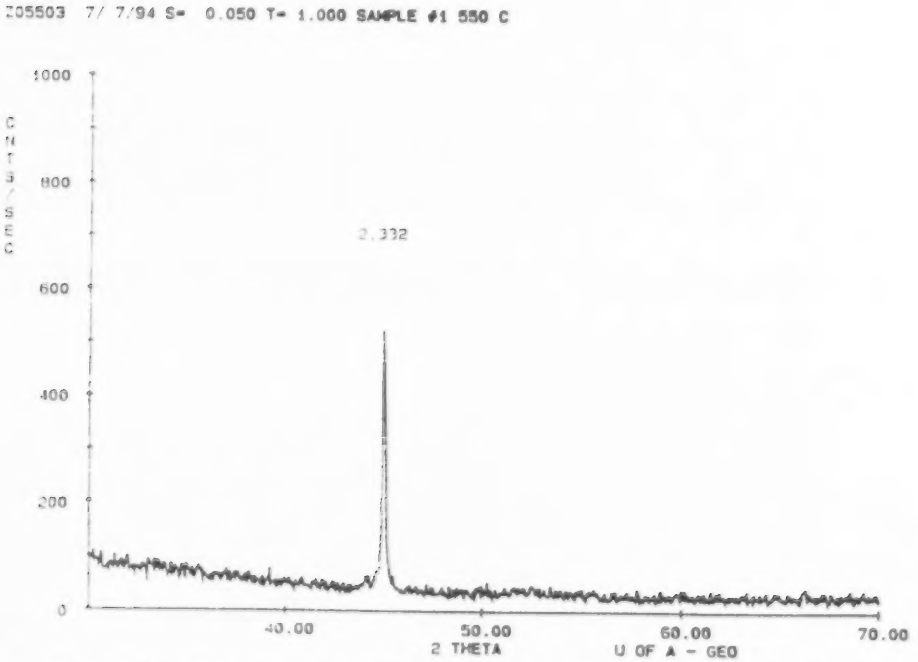

(c)

Figure 3.7 Expanded XRD scan of three aluminum films sputtered at a) room temperature, b) 300 °C, and c) 550 °C.

on the RT film suggests a very low level of oxygen and water vapour during its deposition [42, 43]. The disappearance of the <200> peak on both 300 °C and 550 °C films is due to an annealing effect at the high substrate temperature.

3.1.5 Stress

For studying stress, aluminum films were sputtered on the overhang structure described in section 2.4.1. Figure 3.8 shows a micrograph of an overhang structure with a compressively stressed film deposited on it. For a film in compression, the overhang structure will bend downward due to the expanding force acting on it at the interface between the silicon dioxide and the sputtered film. Likewise, the overhang structure will bend upward for a tensile stress. Results for aluminum films at 3 temperatures are shown in Figure 3.9. After viewing a large collection of overhangs, no significant bending was observed for both room temperature and 550 °C deposited films and a small bending only was observed on the 300 °C films. The film stress, s, was calculated using [63, 64]:

$$s = \frac{\delta}{3L^2 t_f (t_f + t_s)} \left[\frac{E_f t_f^3}{(1-\nu_f)} + \frac{E_s t_s^3}{(1-\nu_s)} \right] \tag{3.2}$$

where δ is the displacement at the end of the overhang and E, t, and ν are the Young's modulus, layer thickness, and Poisson's ratio of the layer and the subscripts s and f denote the aluminum film and the SiO_2 layer.

Although no deflections were observed on the RT and 550 °C films, the limited resolution of the micrographs hinders the detection of low stresses. The resolution of the

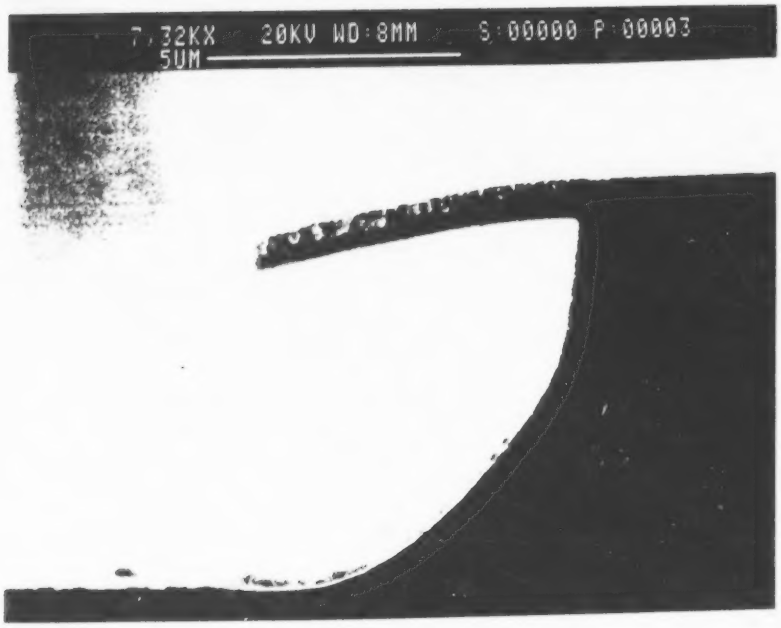

Figure 3.8 A film in compressive stress on top of an silicon dioxide overhang.

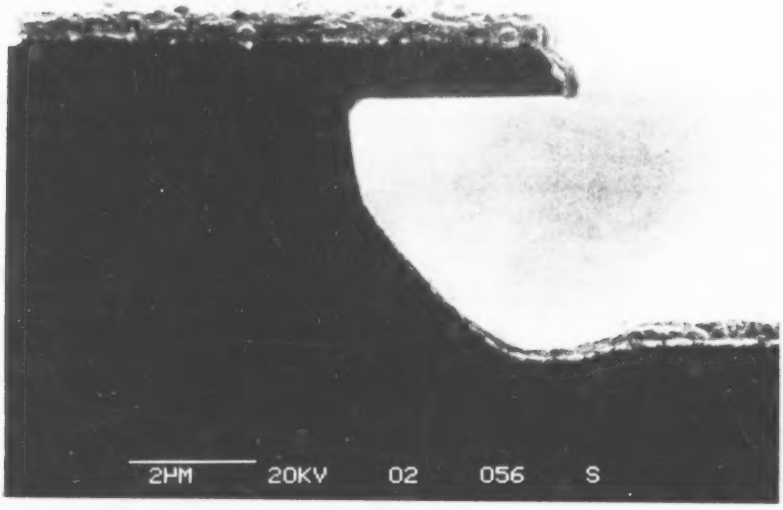

a)

(figure continued ...)

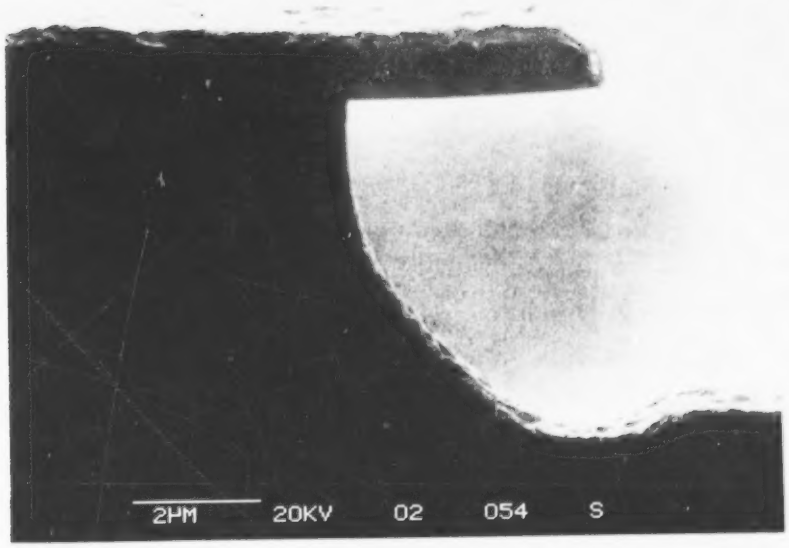

b)

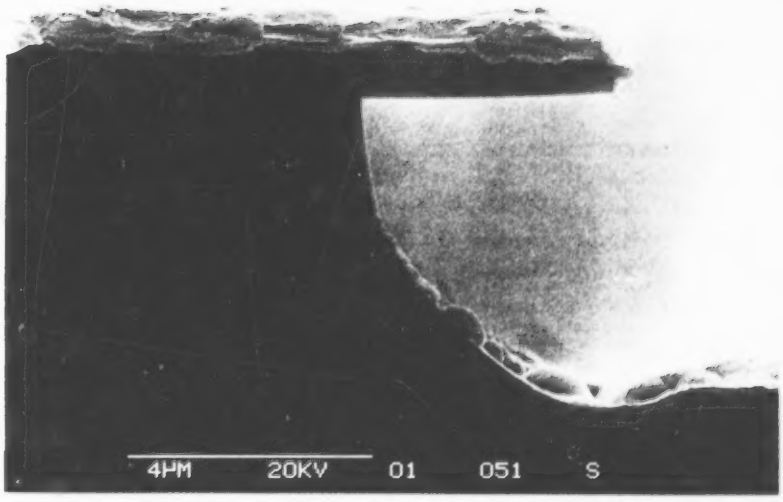

c)

Figure 3.9 Aluminum films deposited on overhang structures at a) RT, b) 300 °C, and c) 550 °C.

micrographs is 10 nm which implies that the uncertainty on the bending measurement is 10 nm either upward or downward. The resulting uncertainty on the stress measurement is 13 MPa or 20 percent error for the 300 °C film. The stress values for each film are listed in Table 3.3.

Table 3.3 Film stress calculated from the overhang experiments.

Deposition temperature	δ (nm)	L (μm)	t_f (μm)	t_s (μm)	Stress σ (MPa)
RT (20 °C)	0	4.2	0.8	0.8	0 ± 13
300 °C	50	4.2	0.8	0.8	65 ± 13
550 °C	0	4.2	0.8	0.8	0 ± 13

$E_f = 0.70 \times 10^{11}$ Pa and $\nu_f = 0.345$ for aluminum.
$E_s = 0.55 \times 10^{11}$ Pa and $\nu_s = 0.16$ for SiO_2.
The measurement errors on δ, L, t_f, and t_s are 10 nm.

General film stresses includes both intrinsic and thermal components [65]. The intrinsic stress is created by the bombardment of energetic particles on the growing films during non-equilibrium film growth. The extrinsic stress is due to the difference of thermal expansion coefficients between the film and the substrate and the response to the change between the deposition temperature and room temperature. Films deposited near or above $T/T_m = 0.3$ should not suffer much intrinsic stress because of crystal relaxation at high substrate temperatures [65]. Even at room temperature, the deposition temperature, 300 K (27 °C), is about one third of the melting point of aluminum which is 933 K (660 °C). Therefore, the three aluminum films deposited in this experiment should have a very low level of intrinsic stress. Since no temperature change occurred on the RT deposited film, the film experiences only intrinsic stress which is 0 ± 13 MPa. Therefore intrinsic stress has only a minor role on the aluminum films deposited under the studied conditions.

Thermal stress is the dominant component for aluminum films deposited at a high temperature because the thermal expansion coefficients of SiO_2 (0.55×10^{-6} /°C) and aluminum (25×10^{-6} /°C) are largely mismatched. Another factor is the elevated deposition temperature for the 300 °C and 550 °C films. If thermal stress was the primary component on the films deposited here, the 550 °C films would have the highest level of stress. However, Ono and *et al.*[66] reported that the film stress of high temperature sputtered aluminum films increased with substrate temperature, but dropped abruptly when film was deposited at 500 °C. It is believed that the high thermal stress on the films above 500 °C exceeds the ultimate tensile stress of aluminum and leads to stress relaxation by plastic deformation. The negligible stress on the 550 °C films agrees with the results of Ono *et al.*.

3.1.5 Summary

Aluminum film coverage over topography improves with increasing substrate temperature, as expected. For RT films, shadowing effects dominated and the coverages on the side-wall and the bottom of trenches were very low. For higher substrate temperatures, the higher adatom mobility lowered the surface curvature and leads to improved coverage over trenches. As a result of the high adatom mobility, the best coverages were achieved at the 550°C film.

The aluminum grain size increases exponentially with the deposition temperature and had values of 1.4, 0.47, and 0.14 μm for the deposition temperatures of 550 °C, 300 °C and RT, respectively. The larger grain sizes and the strong <111> orientation of high

temperature deposited aluminum are advantageous for electromigration resistance. Also, the strong <111> orientations for the three films suggest that the partial pressure of water vapour and oxygen were very low during sputtering. This is to be expected from a UHV process.

Films deposited at the 3 temperatures showed low stress levels. The RT films have no detectable stress because of the small temperature difference between the deposition temperature and room temperature. The film with the highest level of stress is the 300 °C film (65 MPa). No stresses were observed on the 550 °C films presumably because of stress relaxation at temperatures above 500 °C.

The improved coverage over topography, larger grain size, low stress, and strong <111> crystal orientation of high temperature deposited aluminum film indicate that the 'hot' sputtered aluminum is a better technique for metallization than aluminum sputtered without substrate heating.

3.2 3-Step Deposition

The 3-step deposition approach was expected to be the remedy for the wetting problem that is observed by some [44, 59] in 1-step high temperature aluminum. Figure 3.10 shows 3-step and 1-step 550 °C deposited aluminum films on several oxide trenches. The surfaces of the 3-step films are very rough with many hillocks. The average grain size is approximately 1 μm in diameter which is comparable to the 1-step 550 °C film. The coverage over the trenches for the 3-step film is not consistent. In some areas, the trenches are almost completely filled, but the coverage is almost zero in some other areas.

The opening of the smallest trench in Figure 3.10 is sealed off by the aluminum, leaving a void within the trench.

The roughness on the 3-step film suggests the presence of high water or oxygen partial pressure during the deposition. Although the system was evacuated to a UHV level of vacuum prior to deposition and additionally pumped by the cold shroud during deposition, the sudden burst of outgassing from the substrate holder and the substrate during the substrate heating phase may have flooded the region in front of the substrate with water vapour during deposition. Although the 1-step 550°C film was sputtered at high temperature throughout the deposition, the extended baking on the substrate and the holder before deposition reduced the level of outgassing. In comparison, for the 3-step process the sudden (intentional) ramping of temperature may have triggered substantial outgassing.

In addition to the abrupt temperature rise, the heater itself is heated to much higher temperature than 550 °C to achieve a fast temperature rise on the substrate. The heater temperature was not monitored, but an estimate on its temperature can be done by comparing the heater current for maintaining a fixed substrate temperature with the full load heater current. The required heater current for sustaining the substrate temperature at 550 °C is only 40 % of the maximum output current; therefore, the heater temperature at the maximum rated current of 10 A could be as high as 750 °C or above. Since outgassing is a thermally activated process and has little relation to the level of vacuum in

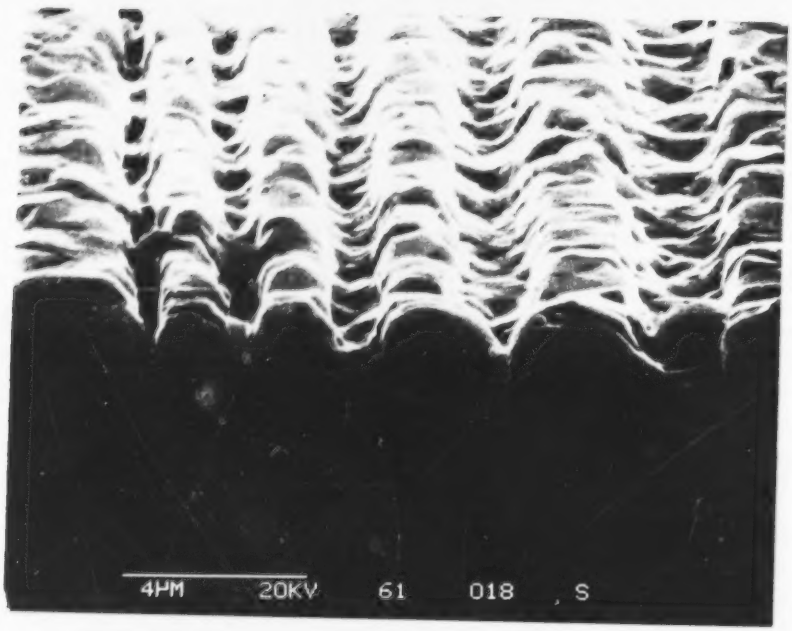

(a)

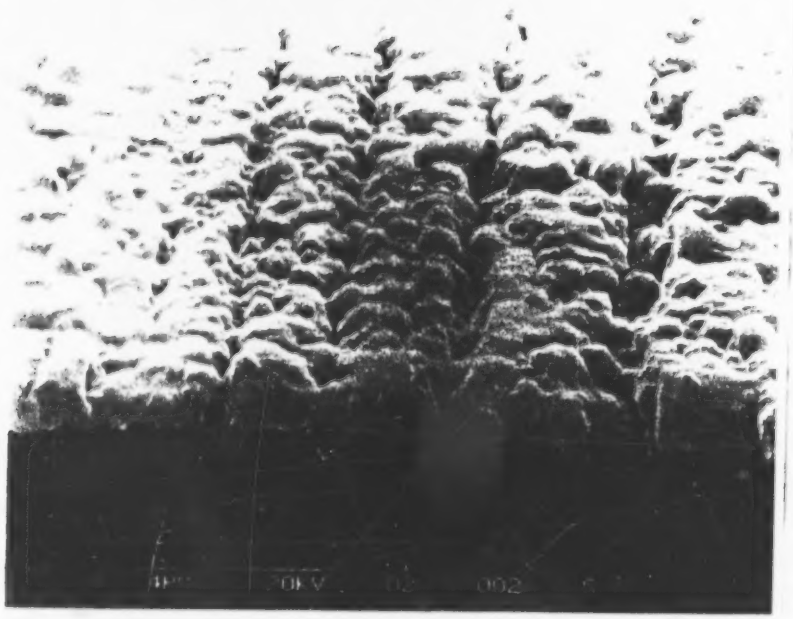

(b)

Figure 3.10 The angle views of high temperature deposited aluminum on trenches by the a) 1-step and b) 3-step methods.

the system [57], the sudden rise of both the heater and substrate temperatures intensified the outgassing.

In terms of film coverage, the 1-step high temperature films are more consistent than the 3-step processed films. As a result of the outgassing during temperature ramping, the film topography of the 3-step process is much rougher than the 1-step process. The rougher film surface contributed to more local shadowing. However, without good monitoring of the residual gases in the deposition chamber during the sputtering, the quality of films deposited by the 1-step and 3-step methods is difficult to compare directly. However, the 1-step method is definitely better than the 3-step in terms of process simplicity.

3.3 2- and 3-dimensional Effects

A 2-dimensional topography structure, a trench, is discussed in previous sections, but most of the features on an IC are 3-dimensional. Cross-sectional views of 1-step and 3-step deposited hot aluminum films on 3-D vias are shown in Figure 3.11. Inadequate wetting of the side-wall dominated the 1-step film and in some areas no aluminum was deposited on the side-walls. Another distinct characteristic of the 1-step film is the asymmetric coating on the vias. The asymmetry is caused by the uneven distribution and the randomness of initial nuclei formation on the via. Following initial nucleation, a growing nuclei intercepts the sputtered flux and grows larger at the expense of other areas. As the grains on the top of the vias continued to grow, eventually the via is sealed off with void formation beneath.

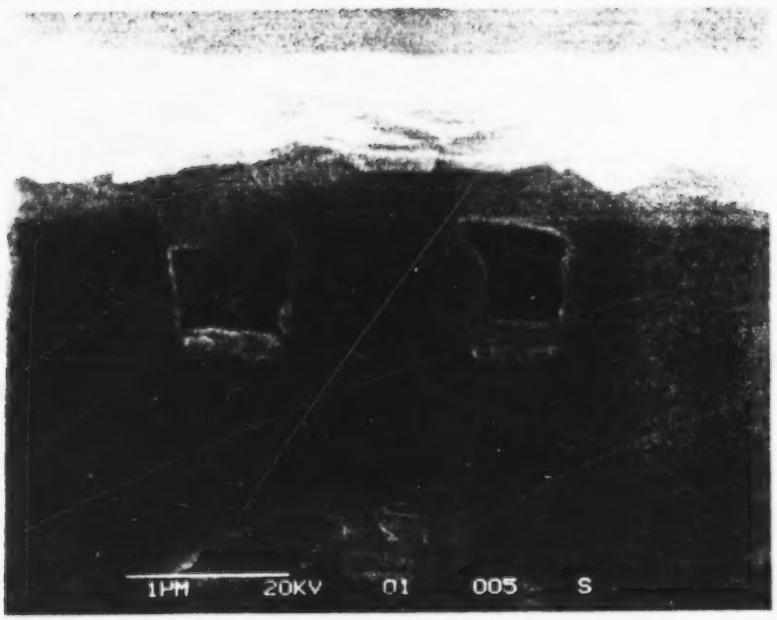

(a)

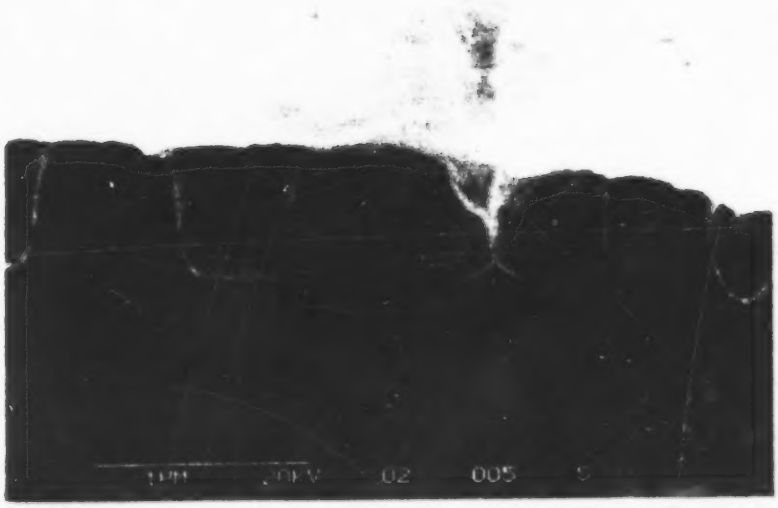

(b)

Figure 3.11 The cross-sectional views of aluminum deposited on vias by the a) 1-step and b) 3-step methods.

The 3-step method was originally designed to overcome the wetting problem of the 1-step method. As shown in Figure 3.11b, one of the vias is completely filled by the 3-step film, but the other vias are empty. This inconsistency appears also on the 2-D trenches and is believed to be caused by the high level of water vapour during the film growth. In the current experimental setup, the 3-step method is not better than the 1-step method. However, the occasional filled via in the 3-step method suggests that the 3-step process may have better potential for depositing hot aluminum.

The coverages on vias are much less than the coverages on the trenches on the NT die for both 1-step and 3-step films. The reduction of film coverage on vias is due to the additional shadowing effect from the third dimension, and self-shadowing. In 2-D trenches only, aluminum is able to flow along the trench and thus fill up a void region, lessening the likelihood of void and asymmetric growth.

3.5 Summary

The high temperature 1-step aluminum process provided a superior coverage on trenches and its film characteristics suggest that its electromigration resistance will be much improved over films deposited at lower temperatures. The 3-step deposition method improved the coverage in some areas of the die, but lacked consistency. The inconsistency is suspected to be caused by the outgassing of water vapour due to abrupt heating of the substrate holder assembly. The filling of 3-D vias is much less than the filling of 2-D trenches, due largely to the additional shadowing by the third dimension.

Chapter 4 : Simulations

Two software packages, SIMSPUD and SIMBAD, were utilized for simulating the 1-step deposited films. SIMSPUD simulates the generation and transport of sputtered flux and SIMBAD simulates the film growth process. The details of these two packages are described in Section 4.1 and 4.2. The extraction of the parameters required for the simulations is explained in Section 4.3. The discussion on the simulation results from SIMSPUD and SIMBAD is presented in Sections 4.4 and 4.5.

4.1 Sputter Flux Simulation

SIMSPUD is a three dimensional Monte Carlo simulation for modelling the transport of sputtered atoms from a target to a substrate. Figure 4.1 is a schematic of SIMSPUD model. For the first phase of the simulation, the emission of a sputtered atom is generated based on the erosion profile of the target. A high probability of emitting a sputtered atom is assigned to the heavily eroded regions. The second phase simulates the interaction between the sputtered atoms and the sputtering gas. Many collisions occur between the sputtered atoms and the sputtering gas before the atoms arrive on the substrate, altering the paths and trajectories of the atoms. The collision cross-section between the sputtered atom and the sputtering gas is an input to the simulation for proper modelling of the collision process. Finally, the impact trajectory of each simulated atom is collected for generating the angular distribution of the sputtered flux and the relative thickness profile of the sputtered film. The extraction of target erosion profile and collision cross-section is described in Section 4.3.1 and 4.3.2.

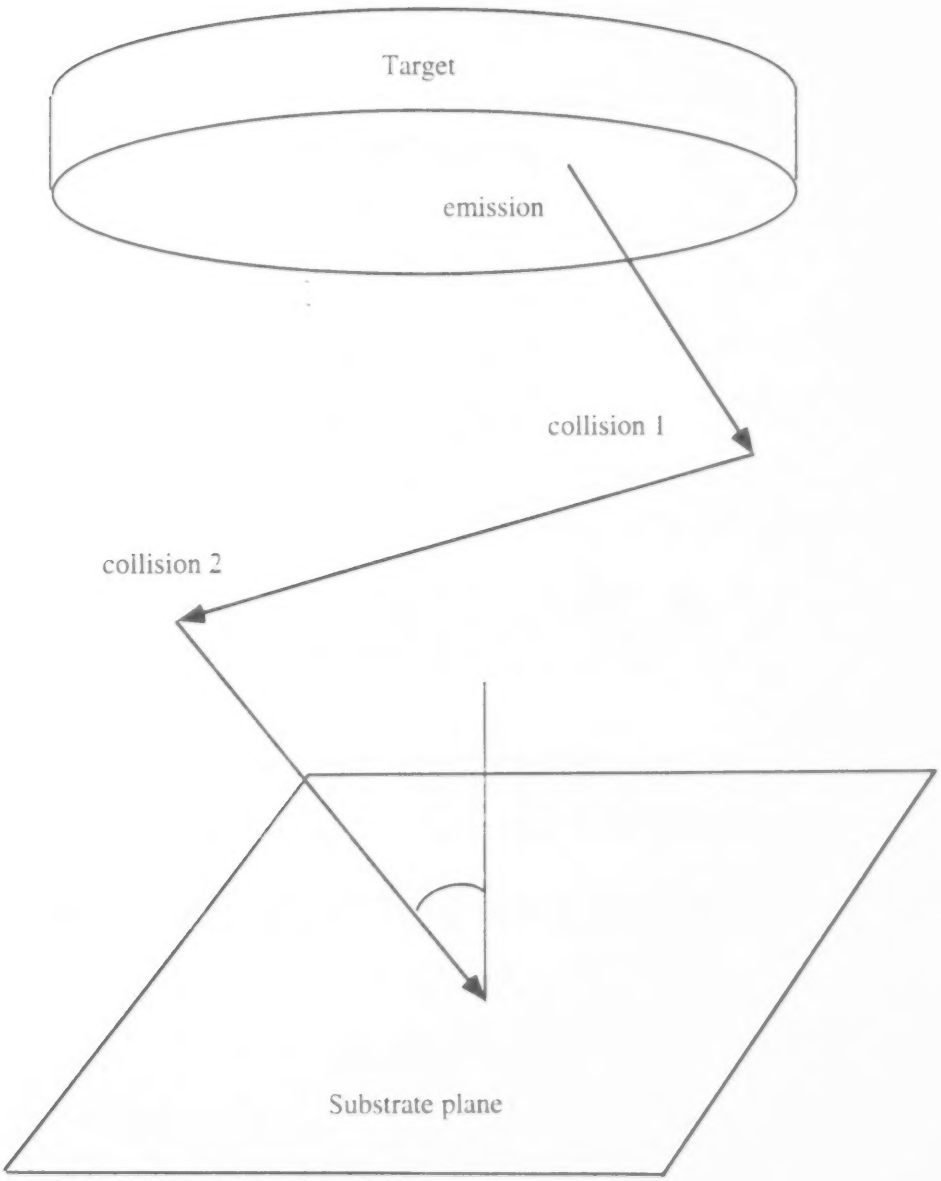

Figure 4.1 SIMSPUD simulation sequence for sputtered flux vapour transport [52].

4.2 Film Growth Simulation

SIMBAD simulates the film growth process by two stages. The first stage determines the impact site of the material. Two-dimensional hard discs are launched above the substrate plane, representing a large collection of sputtered atoms with similar trajectories. The discs follow a straight line trajectory until hitting the substrate or a previously deposited disc (film surface). The trajectories of the discs are based on the angular distribution determined by SIMSPUD. During the second stage, the resting sites for the discs are computed based on the minimization of surface potential. The SIMBAD simulation sequence is illustrated in Figure 4.2.

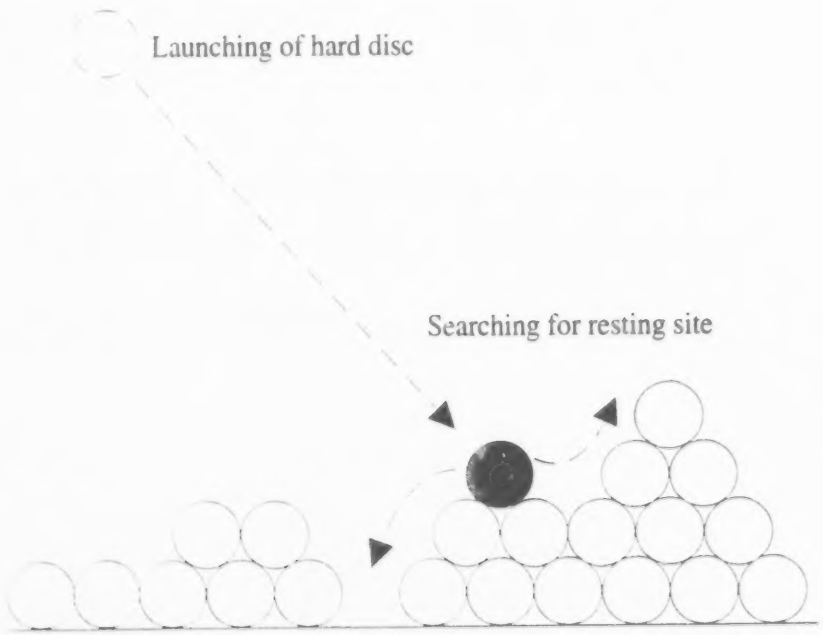

Figure 4.2 Film grow process simulated by SIMBAD [52].

The surface potential of a two dimensional surface can be expressed as [67]:

$$\mu = \mu_0 + \frac{\gamma}{R}\Omega \tag{4.1}$$

where μ_0 is the chemical potential of a flat surface; γ is the surface tension; R is the radius of curvature; and Ω is the atomic volume. Since μ_0, γ, and Ω are fixed for a given material, the term 1/R is the only variable left to minimize. In SIMSPUD, R is defined as $ds/d\alpha$ where $d\alpha$ is the change in surface normal and ds is the displacement along the surface. The search for minimum surface potential is confined within the surface diffusion length specified by the user.

As noted earlier, the surface diffusion length is a strong function of the substrate temperature and can be expressed as [53]:

$$L = \sqrt{D_0 \tau}\exp(-Q_s / 2k_B T) \tag{4.2}$$

where D_0 is the surface diffusion constant; τ is the average length of time an adatom remains mobile on the film surface; Q_s is the activation energy for surface diffusion; k_B is the Boltzmann constant; and T is the substrate temperature. Although the expression for L is known, the factors $\sqrt{D_0 \tau}$ and Q_s are not well defined. $\sqrt{D_0 \tau}$ is a strong function of deposition and surface conditions and is very difficult to measure and quantify. Q_s has been reported with different values [68, 69]. Therefore, the surface diffusion lengths for the three sets of 1-step deposited films are evaluated by matching simulation and experimental results. The details of determining the surface diffusion lengths are discussed in Section 4.5.

4.3 Extraction of Simulation Parameters

The majority of the simulation parameters were collected from the literature. Several parameters are strongly related to the sputtering system and experimental setup and have to be provided to calibrate the package to individual systems. Those parameters are the target erosion profile of the sputtering target, the collision cross-section between the sputtered atoms and sputtering gas, and the sticking coefficient of the sputtered material on the substrate.

4.3.1 Target Erosion Profile

The target erosion profile depends strongly on the geometry and the magnetic field strength of the magnetron. The magnetic field confines the plasma and leads to uneven erosion across the target. To accurately compute the emission distribution of sputtered atoms, an erosion profile must be measured and input to SIMSPUD for the system under simulation.

The target erosion profile used in the experiments was measured by a profiler which is a comb with an array of retractable pins. The profiler was pushed against the target and the retractable pins repositioned themselves to conform with the contour of the target. The erosion profile was obtained by measuring the retraction of each pin. A new 2-inch target was sputtered for more than 10 hours before measurement of the erosion profile to ensure a representative erosion on the target. The measured profile is shown in Figure 4.3.

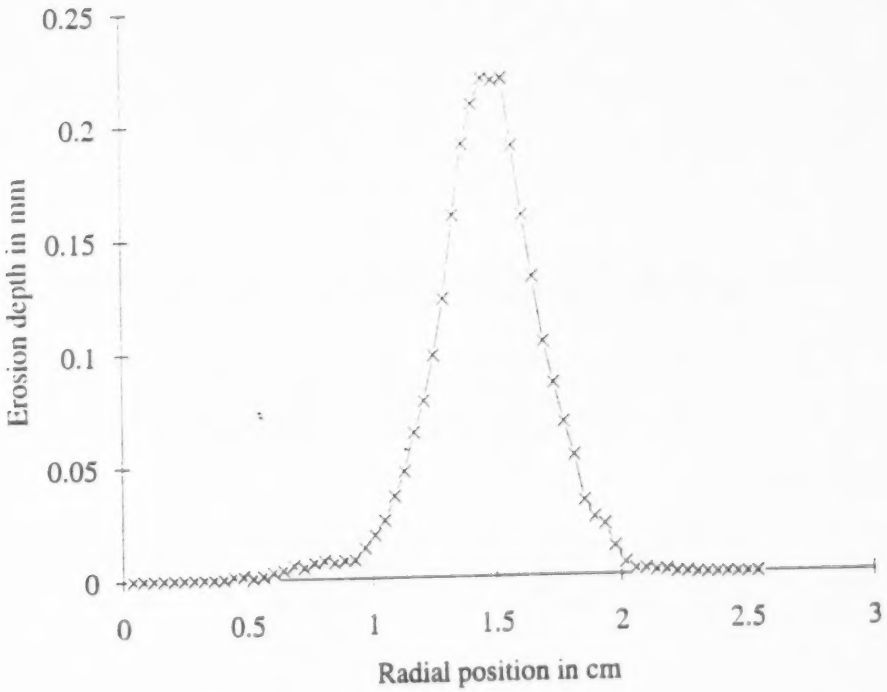

Figure 4.3 Erosion profile of the 2-inch aluminum target

4.3.2 Collision Cross-section

Another important parameter for SIMSPUD is the collision cross-section of the sputtered atoms with the sputtering gas. In the simulation, the amount of interaction between the sputtered atoms and the sputtering gas is determined by the collision cross-section input by the user. This cross-section varies greatly with the atom's energy. In SIMSPUD, the cross-section (σ) is empirically fitted to the energy dependence of the cross-section reported by Robinson[70]. For the empirical fitting, only two parameters are required to characterize the energy dependence. They are the cross-section (σ_t) of

thermalized metal atoms with energy (E) below 1 eV and the coefficient (σ_0) for the fitting equation (see Eq. 4.3) for energetic atoms with energy above 1 eV.

$$\sigma(E) = \sigma_t, \qquad E < 1\ eV \tag{4.3a}$$

$$\sigma(E) = \sigma_0 E^{-0.29}, \quad E \geq 1\ eV \qquad \text{(where E is in eV)} \tag{4.3b}$$

To calibrate the cross-section, the simulated angular distribution was compared with the distribution obtained by a pinhole experiment. The calibration was previously carried out by Dew *et al.* [52]. The values for aluminum are $\sigma_0 = 45$ Å^2 and $\sigma_t = 60$ Å^2.

4.3.3 Sticking Coefficient

If the sticking coefficient is less than unity, some of the deposited atoms will reflect from the original impact site and redeposit elsewhere. Since this redistribution will affect coverage profiles, it is important to have a knowledge of the sticking coefficient for film growth simulations. To verify that the sticking coefficient of aluminum on the substrate is unity, the overhang experiment for measuring film stress was utilized. With the underside of the overhang facing away from the deposition source, any film accumulated on that side will be an indication of a non-unity sticking coefficient (or significant resputtering).

Figure 4.4 is a high magnification SEM shot of the overhang shown in Figure 3.9b and clearly indicates that no significant amount of material was redeposited on the underside of the overhang. To establish a lower limit of the sticking coefficient due to finite SEM resolution, Figure 4.4 was compared with a set of SIMBAD simulations for

sticking coefficients ranging from 0.9 to 1. Those simulations are shown in Figure 4.5. By comparison with Figure 4.4, the sticking coefficient of the sputtered aluminum is assumed to be greater than 0.99. Therefore, a unity sticking coefficient was used in the simulations for the 1-step deposited films.

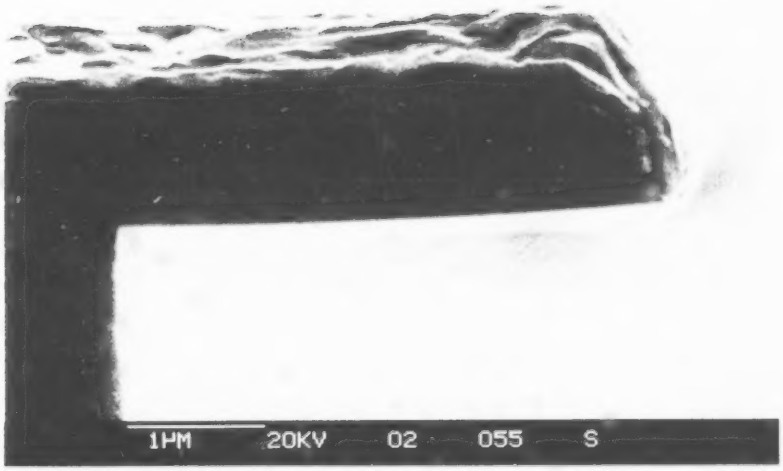

Figure 4.4 High magnification SEM micrograph of the overhang.

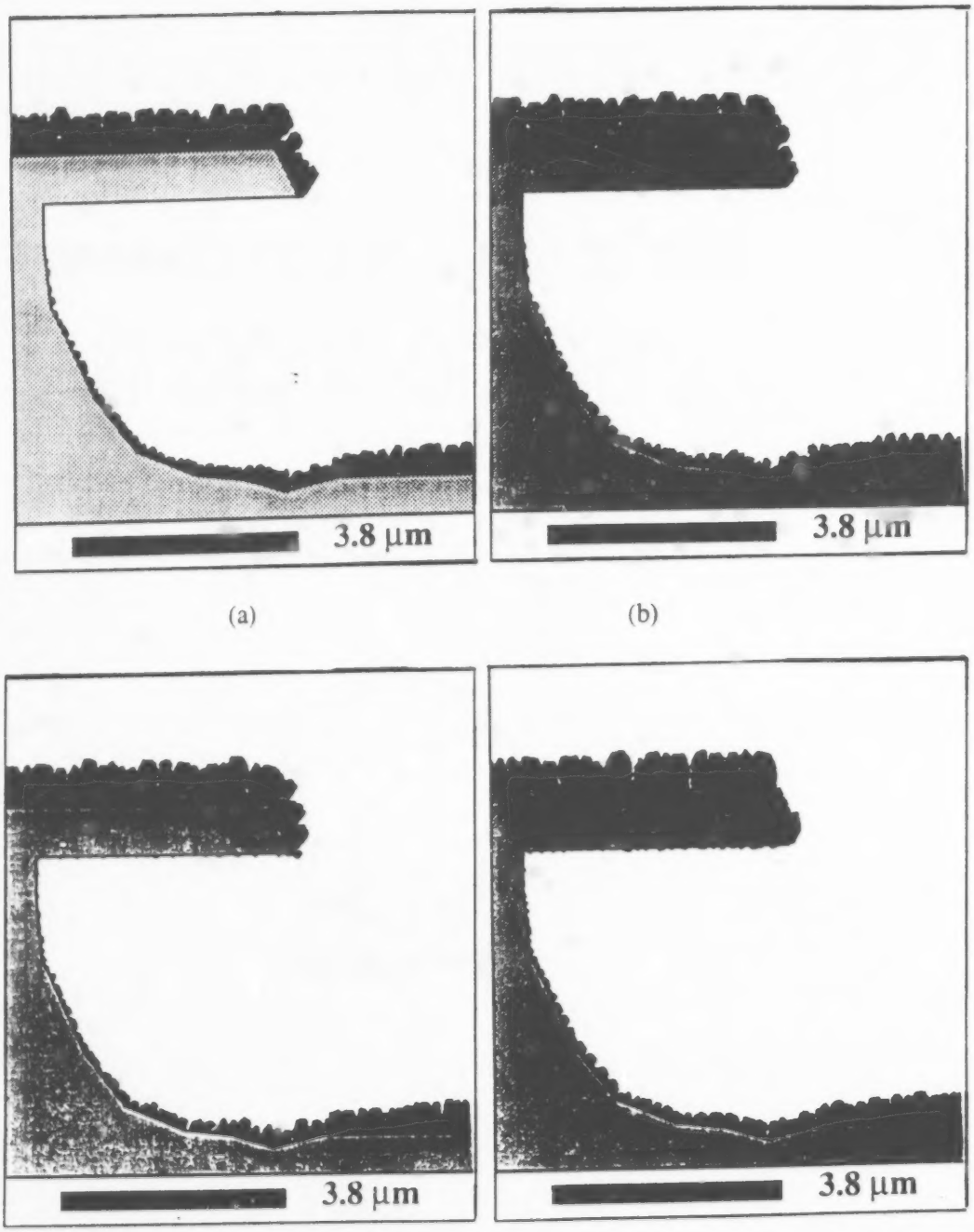

Figure 4.5 SIMBAD simulation of aluminum sputtered on the overhang with sticking coefficients of a) 1.00, b) 0.99, c) 0.95, and d) 0.90.

4.4 Angular Distribution

The determination of the angular distribution by SIMSPUD is a statistical process in which the accuracy improves as more particles are simulated. Figure 4.6a is the angular distribution from a simulation of 100,000 particles transported from the target to the substrate plane. The distribution curve is noisy due to the large uncertainties of the data. To reduce the uncertainties, the number of simulation particles must be increased. Since the uncertainty is inversely proportional to the square root of the number of particles, the number of particles must be increased by 100 to lower the uncertainty by a factor of ten. A typical simulation time with 100,000 particles on a Sparc1+ workstation is about 3 hours. As the simulation time increases linearly with the number of simulation particles, a 10,000,000 particle simulation is expected to take 300 hours or 12.5 days. The long run time is impractical and the program may abort at the middle of the simulation if the computer is interrupted by unexpected events. The alternative is breaking the large simulation into many small simulations and averaging the results.

Three hundred 100,000-particle simulations were run concurrently over 30 Sparc1+ workstations for a 24 hour period. The angular distribution from each simulation was averaged to get the final angular distribution. Each final data point is the average of the corresponding data point over the three hundred simulations and the uncertainty is the root-mean-square of the uncertainties of the simulations divided by the

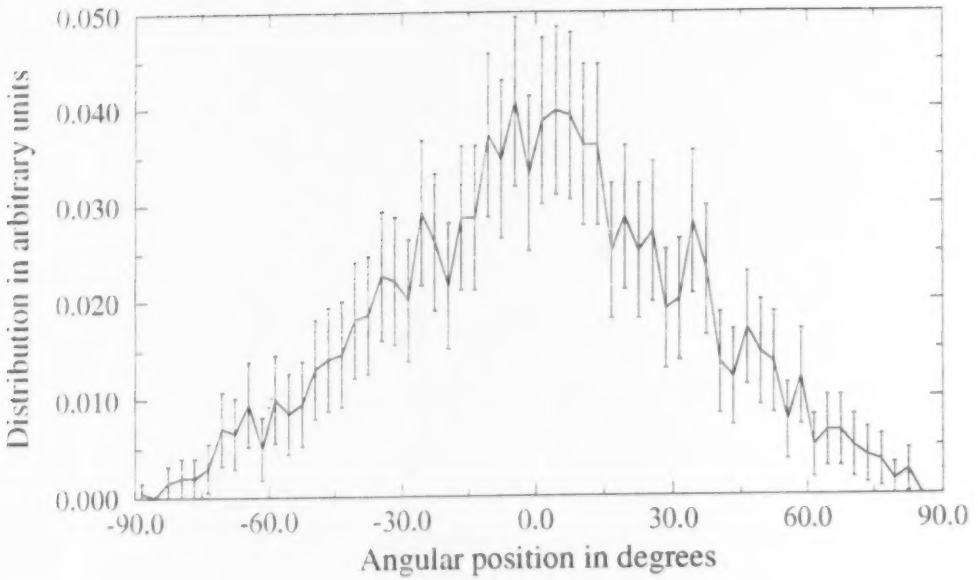

(a)

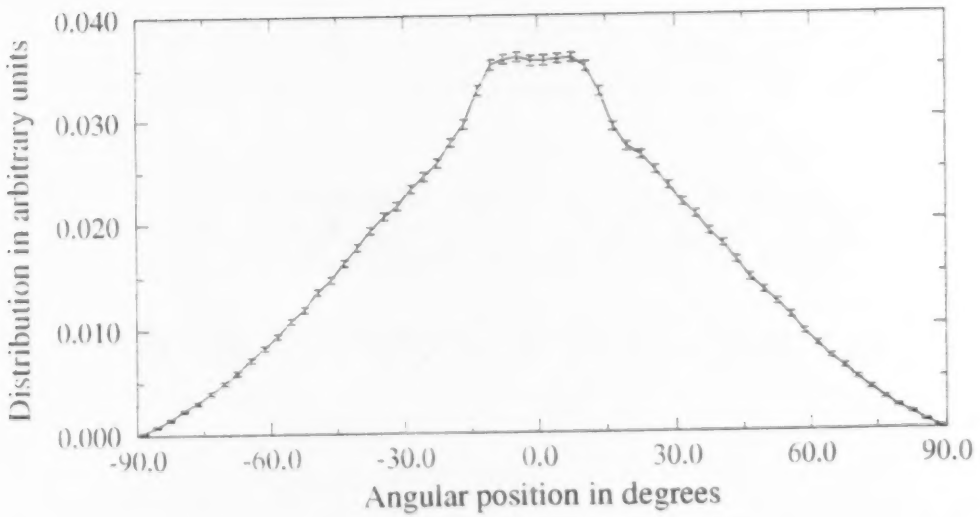

(b)

Figure 4.6 The angular distributions of aluminum film at 10 mT by a) a 100,000-particle simulation and b) averaging over three hundred 100,000-particle simulations.

square root of the number of simulations. These two relationships are shown mathematically below:

$$\bar{x} = \frac{1}{N} \sum x_i \tag{4.4}$$

$$\sigma = \frac{1}{N} \sqrt{\sum \sigma_i^2} = \frac{\sqrt{\frac{1}{N} \sum \sigma_i^2}}{\sqrt{N}} \tag{4.5}$$

where $\bar{x}$ is the average value of the data points, x_i; σ is the uncertainty and N is the number of simulations. The final angular distribution calculated by averaging over three hundred 100,000-particles simulations is shown in Figure 4.6b. The curve in Figure 4.6b is much smoother and symmetrical compared to the curve produced by the 100,000 simulation, and with smaller uncertainties as expected. The angular distribution of Figure 4.6b was used for the film growth simulations in Section 4.5.

The issue of flux acceptance angle is revisited here. The amount of flux deposited at a point can be estimated by integrating the flux angular distribution over the flux acceptance angle. This is shown mathematically in Equation 4.6a:

$$\eta = \int_{\theta_a} \Phi(\theta) d\theta \tag{4.6a}$$

where $\Phi(\theta)$ is the angular distribution of sputtered flux and θ_a is the flux acceptance angle. For a discrete distribution, such as the one in Figure 4.6b, the integration operator is replaced by a summation operator and Eq 4.6a becomes:

$$\eta = \sum_{\theta_a} \Phi_i \tag{4.6b}$$

Since the angular distribution is normalized, the value obtained by Equation 4.6 is the relative flux acceptance for which a unity value represents no obstruction for the sputtered flux. The relative flux acceptance at the lower corner and the centre of a trench is plotted in Figure 4.7. For wide trenches, the flux acceptance is almost unity at the centre, but is only 50 % at the corner. The lower flux acceptance at the corner is due to the shadowing effect of the side-wall which blocks off half of the incoming flux; thus, the flux acceptance at the corner is limited to 50 %.

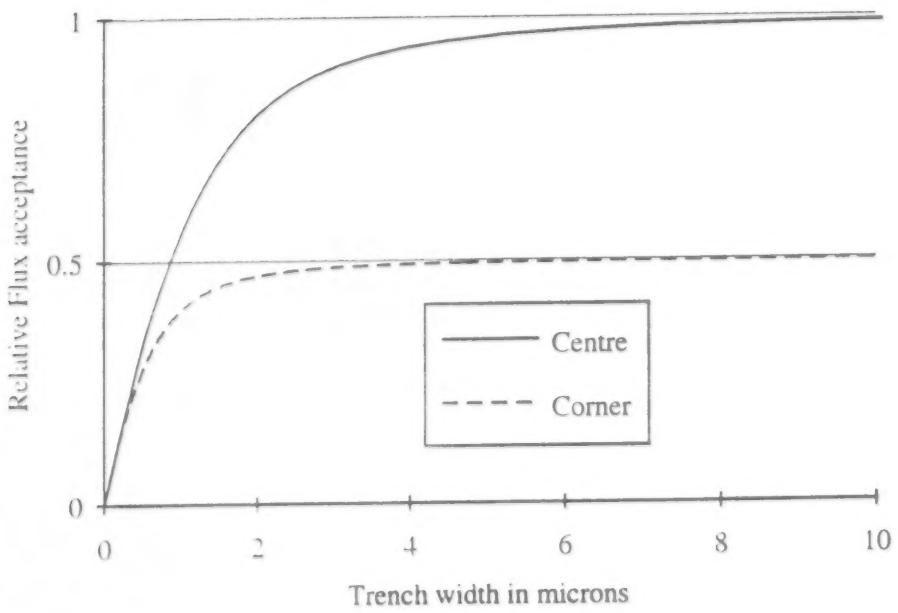

Figure 4.7 The relative flux acceptance at the lower corner and at the centre of a 1-μm deep trench vs. trench width.

The values of relative flux acceptance for 1 μm wide trenches are very different from the bottom and step coverages measured in Chapter 3 because the flux acceptance does not take into account the self-shadowing effect in the low temperature deposited film and the high adatom mobility for the hot aluminum film. A film growth simulator, such as SIMBAD, is required for a more precise measure of the effectiveness for providing coverage over topography by a flux distribution. However, a qualitative estimate of coverage is provided by the flux acceptance.

4.5 1-step Deposited Film Simulation

The surface diffusion length is the critical parameter for simulating films deposited at various substrate temperatures. A series of simulations with different diffusion lengths were compared with the 1-step deposited films to determine the diffusion length for each temperature. The three best matched simulations are shown in Figure 4.8. The diffusion lengths used in those simulations are 0.6 μm, 0.1 μm, and 0.05 μm for 550 °C, 300 °C, and RT films and are plotted in Figure 4.9.

The simulations depict most of the features of the two high temperature films, but were unable to accurately reproduce the profile of the RT film. The tapered trench and 100 percent coverages are clearly shown on the 550 °C film simulation; the rectangular film profile is reproduced on the 300 °C film simulation. However, SIMBAD was unable to depict the distinct overhang of aluminum film on the edge of the oxide step. The

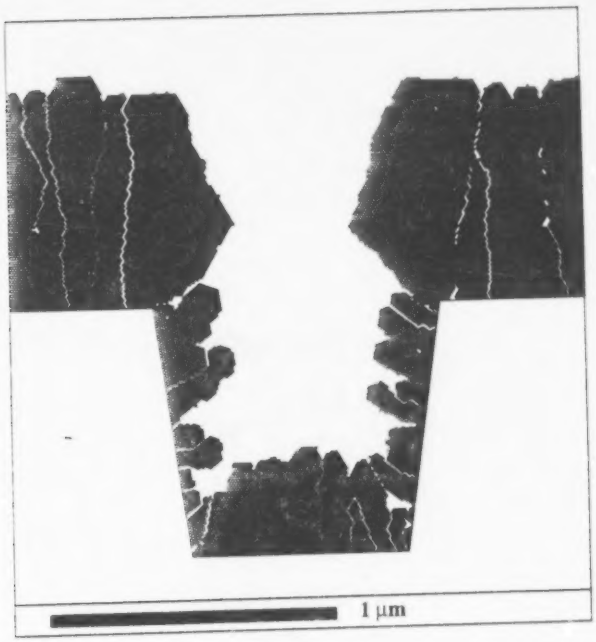

(a)

(b)

Figure 4.8 SIMBAD depictions of aluminum films deposited at a)RT, b) 300 °C, and c) 550 °C.

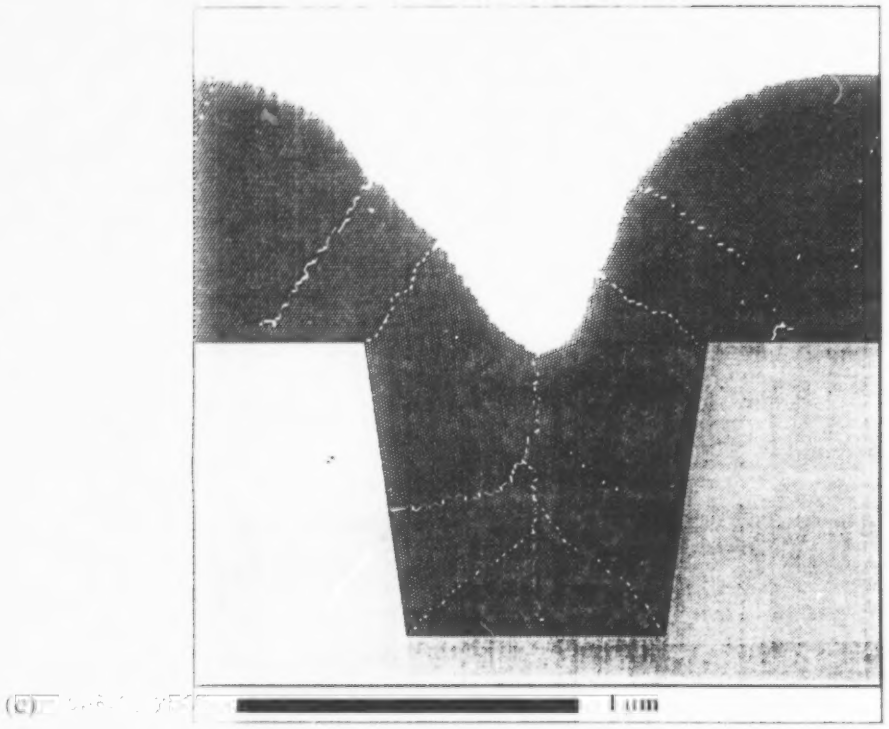

Figure 4.8 SIMBAD depictions of aluminum films deposited at a) RT, b) 300 °C, and c) 550 °C.

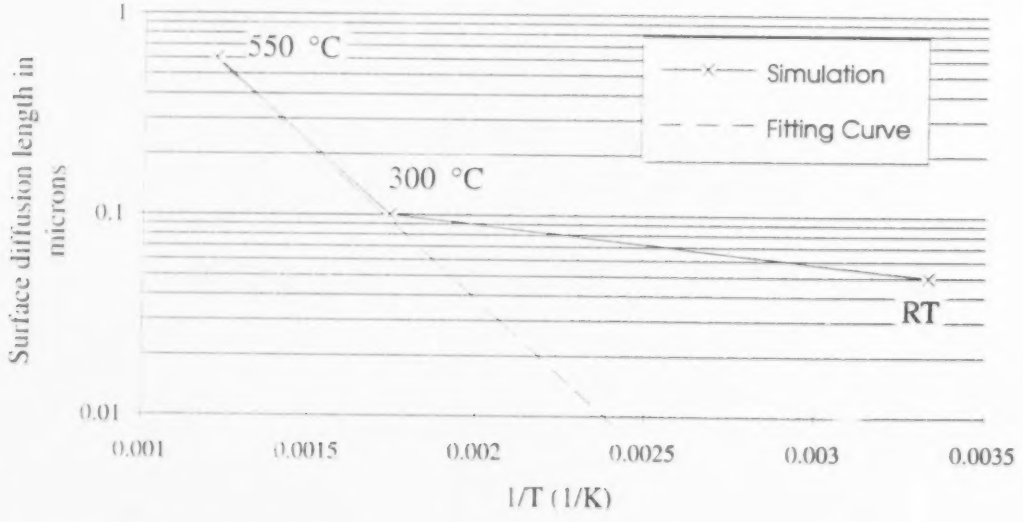

Figure 4.9 Surface diffusion length obtained from simulations for various substrate temperatures. The dotted line is the fitting curve based on the extracted parameters $\sqrt{D_s \tau}$ and Q_s.

failure of simulating the RT film could be caused by factors not currently considered by SIMBAD.

One possible cause of the lack of agreement at RT is the asymmetric diffusion length of adatoms due to the high impact energy. When a sputtered atom impacts on a sloped surface on the edge of oxide step, the adatom may skip forward before finally bonding on the substrate. This skipping action effectively increases the surface diffusion length in the forward direction and reduces the surface diffusion length in the backward direction. Consequently, more material would deposited over the oxide edge and an overhang feature would be formed. This process has little effect on film simulations at high temperatures due to the relatively long surface diffusion length.

As discussed in section 4.2, the surface diffusion length of adatoms is related to the substrate temperature by Equation 4.2. The parameters $\sqrt{D_0\tau}$ and Q_s in the surface diffusion length equation were calculated from the diffusion length obtained from film simulations by the following two equations.

$$Q_s = \frac{2k}{\left(\frac{1}{T_2} - \frac{1}{T_1}\right)} \ln\left(\frac{L_1}{L_2}\right) \tag{4.7}$$

$$\sqrt{D_0\tau} = \frac{L_1 - L_2}{\exp\left(\frac{-Q_s}{2kT_1}\right) - \exp\left(\frac{-Q_s}{2kT_2}\right)} \tag{4.8}$$

where L is the surface diffusion length with subscripts 1 and 2 denoting two different

substrate temperatures. L values obtained from the 550 °C and 300 °C simulations were used for calculating $\sqrt{D_o\tau}$ and Q_s. L from the RT film simulation was ignored in the calculation because the actual surface temperature of the RT film during deposition was unknown. $\sqrt{D_o\tau}$ and Q_s found to be 36 μm and 0.58 eV, respectively. The value of Q_s is comparable with 0.4 eV reported by Neumann and Hirschwald [68] and 0.45 eV reported by Cale [69]. However, the value of $\sqrt{D_o\tau}$ is highly dependent on deposition conditions and the surface conditions of substrates. Therefore, no attempts were made to compare the calculated $\sqrt{D_o\tau}$ with values reported by others.

After obtaining the values of $\sqrt{D_o\tau}$ and Q_s, the diffusion length of films deposited at other temperatures can be obtained and are plotted on Figure 4.9 along with *L* values obtained from simulations. The fitted curve falls away from the data point obtained from RT films. This discrepancy is due to the small number of data points for determining $\sqrt{D_o\tau}$ and Q_s and the unknown substrate temperature on the RT films. Although the fitting curve and RT data do not agree, diffusion lengths obtained from interpolating the two high temperature diffusion lengths by the fitting curve should be valid. Simulations of films deposited at other high temperatures are possible once the behaviour of L is determined.

In summary, SIMBAD successfully depicted the profiles of the two high temperature sputtered films, but was unable to simulate the overhang feature on the RT films. Not accounting for a biased diffusion length in the direction of an incoming energetic adatom may be the cause of the failure on the RT film simulations. Further

modifications to the code to include the effect of a biased diffusion length may remedy this problem.

Chapter 5 : Conclusion

Aluminum films were sputtered onto heated substrates by 1-step and 3-step processes. The films were characterized by their grain sizes, crystal orientations, stresses ! coverage over topography. Also, the films were simulated using the SIMBAD and SIMSPUD models.

From the 1-step process, larger grain, improved coverage, and strong <111> crystal orientation films were found when substrates were heated. Film stresses were very low for the aluminum films, but the low sensitivity of the overhang structure hindered the detection of film stresses less than 13 MPa. For further experiments, longer and thinner overhang structures should be used to enhance the sensitivity of stress measurements.

For both 1-step and 3-step deposited films, the coverages on vias were not as good as on trenches because of the shadowing effect from the third dimension. Problems associated with irregular wetting were most noticeable on the 1-step films. In contrast, the 3-step process filled a few vias, but was not consistent over a die. Outgassing during deposition is believed to be the cause of the greater film roughness and the inconsistency in the 3-step process. However, the fact that a few vias were filled successfully suggests that the 3-step process may have a better potential for depositing hot aluminum.

SIMBAD successfully predicted film profiles for the two high temperature 1-step films. It depicted the dominant features of those films, such as the tapered side-walls on the 550 °C films and the rectangular trench on the 300 °C films. This is the first direct

evidence verifying SIMBAD predictions of high temperature sputtering. However, SIMBAD was unable to precisely predict the film profile on RT films. A possible cause of the disagreement between SIMBAD and the RT films is a directionally biased surface diffusion length in the direction of the incident adatom's velocity. This biased diffusion length would not affect high temperature deposited films because the temperature activated diffusion length is much greater than the bias diffusion length shift. A model for the biased diffusion length is currently under development.

From comparison of simulation and experiment, the two parameters, $\sqrt{D_o \tau}$ and activation energy, Q_s, for surface diffusion were determined and found to be 38 μm and 0.59 eV, respectively. Although the experimental data is limited and the substrate temperatures on RT film were uncertain, the inferred activation energy is comparable with values reported by others.

If work were to continue, it is recommended that better substrate temperature monitoring be employed, such as embedding a thermistor on the substrate for in situ temperature measurement. Also, films should be deposited at a wider range of temperatures to enrich experimental results and improve the accuracy of the determination of the surface diffusion length.

References

[1] J.E. Kelly, D.J. Fleming, "Interconnection Technology and Manufacturability Issues", Advanced Metallization for ULSI Applications Conference Proceedings, 1992, p.13.

[2] C. Hu, "MOSFET Scaling in the Next Decade and Beyond", Semiconductor International, June 1994, p. 105.

[3] D. Pramanik, A.N. Saxena, "VLSI Metallization Using Aluminum and its Alloys, Part II", Solid State Technology, March 1983, p.131.

[4] A.K. Sinha, "Metallization Technology for Very-Large-Scale Integration Circuits", Thin Solid Films, Vol. 90, 1982, p. 271.

[5] R.J. Holwill, "The Current Status of Metallization in Integrated Circuit Applications", Materials Science and Engineering A, Vol. 116, 1989, p. 143.

[6] A.G. Sabnis, "Metal Electromigration", VLSI Electronics Microstructure Science, edited by N.G. Einspruch, Academic Press, San Diego, 1990, p. 53.

[7] S.P. Murarka, "Interactions in Metallization Systems for Integrated Circuits", Journal of Vacuum Science Technology B, Vol. 2, No. 4, 1984, p. 693.

[8] J.R. Black, "Electromigration-A Brief Survey and Some Recent Results", IEEE Transactions on Electron Devices, Vol. 16, 1969, p. 338.

[9] X. Gui, Steven K. Dew, and M.J. Brett, "Three-Dimensional Thermal Analysis of High Density Triple-Level Interconnection Structures in Very Large Scale Integrated Circuits", Journal of Vacuum Science Technology B, Vol. 12, No. 1, P. 59-62, 1994.

[10] T. Smy, D. J. Reny, and M. J. Brett, "Simulation of the Effect of Thin Film Microstructure on Current and Temperature Distributions in Very Large Scale Integrated Metallization Structures", Journal of Vacuum Science and Technology B, Vol. 10, No. 5, 1992, p. 2267.

[11] W. Allegretto, A. Nathan, K Chau, and H.P. Baltes, "Two-Dimensional Numerical Simulations of Electrothermal Behaviour in Very Large Scale Integrated Contacts and Vias", Canadian Journal of Physics, Vol. 67, 1989, p. 212.

[12] J.T. Trattles, A.G. O'Neill, and B.C. Mecrow, "Three-Dimensional Finite-Element Investigation of Current Crowding and Peak Temperatures in VLSI Multilevel Interconnections", IEEE Transactions on Electron Devices, Vol. 40, No. 7, 1993, p. 1344.

[13] J.A. Schwarz, "Electromigration in Interconnects and Contacts", VLSI Electronics 15 - VLSI Metallization, edited by N.G. Einspruch, Academic Press, Orlando, 1987, p. 221.

[14] A. Scorzoni, B. Neri, C. Caprile, and F. Fantini, "Electromigration in Thin-Film interconnection Lines: Models, Methods and Results", Materials Science Reports, Vol. 7, 1991, p. 143.

[15] A.J. Learn, "Evolution and Current Status of Aluminum Metallization", Journal of Electrochemical Society, Vol. 123, No. 6, 1976, p. 894.

[16] S. Vaidya, D.B. Fraser, and A.K. Sinha, "Linewidth Dependence of Electromigration in Evaporated Al-0.5%Cu", Applied Physics Letters, Vol. 36, 1980, p.464.

[17] T. Kwok, "Effect of Metal Line Geometry on Electromigration Lifetime in Al-Cu Submicron Interconnects", Proceedings of 1992 International Reliability Physics Symposium, 1988, p. 185.

[18] D. Pramanik, "VMI Conductor Systems", 1993 VLSI Multilevel Interconnection Tutorial, 1993, p. 115.

[19] D. W. Skelly, T. M. Lu, and D. W. Woodruff, "Metallization Techniques", VLSI Electronics Microstructure Science 15 - VLSI Metallization, edited by N.G. Einspruch, Academic Press, Orlando, 1987, p.101.

[20] B. Chapman, *Glow Discharge Processes*, Wiley, New York, 1980.

[21] S.M. Rossnagel, "Glow Discharge Plasmas and Sources for Etching and Deposition", Thin Film Processes II, edited by J.L. Vossen and W. Kern, Acedemic Press, New York, 1991, p. 11.

[22] J.A. Thornton, "Influence of Apparatus Geometry and Deposition Conditions on the Structure and Topography of Thick Sputtered Coatings", Journal of Vacuum Science and Technology, Vol. 11, No. 4, 1974, p. 666.

[23] J.A. Thornton, "High Rate Thick Film Growth", Annual Review of Material Science, Vol. 7, 1977, p. 239.

[24] J.A. Thornton, "The Microstructure of Sputter-Deposited Coatings", Journal of Vacuum Science and Technology A, Vol. 4, No. 6, 1986, p.3059.

[25] J.A. Thornton, "Structure-Zone Models of Thin Films", Proceedings of SPIE, Vol. 821, 1987, p. 95.

[26] B.A. Nivchan and A.V. Demchishin, "Study of the Study of the Structure and Properties of Thick Vacuum Condensates of Nickel, Titanium, Tungsten, Aluminum Oxide, and Zirconium Dioxide", Fiz. Metal. Metalloved., Vol. 28, No. 4, 1969, p.653.

[27] R.N. Tait, *Thin Film Microstructure Effects in VLSI Metallization*, Ph.D. thesis, Department of Electrical Engineering, University of Alberta, Edmonton, 1992.

[28] A.N. Saxena and D. Pramanik, "VLSI Multilevel Metallization", Solid State Technology, Dec. 1984, p. 93.

[29] Y. Homma and S. Tsunekawa, " Planar Deposition of Aluminum by RF/DC Sputtering with RF Bias", Journal of the Electrochemical Society, Vol. 132, No. 6, 1985, p. 1466.

[30] T. Hariu, K. Watanabe, M. Inoue, T. Takada, and H. Tsuchikawa, "The Properties of Al-Cu/Ti Films Sputter Deposited at Elevated Temperatures and High DC Bias", Proceedings of 1989 International Reliability Physics Symposium, 1989, p. 210.

[31] D. R. Bradbury, J. E. Turner, K. Nauka, and K. Y. Chiu, "Selective CVD Tungsten as an Alternative to Blanket Tungsten for Submicron Plug Applications on VLSI Circuits", IEDM 91, 1991, p. 273.

[32] T. Ohba, M. Shirasaki, N. Misawa, T. Suzuki, T. Hara, and Y. Furumura, "Selective and Blanket Tungsten Interconnection and Its Suitability for 0.2-Micron ULSI", 1990 IEEE VLSI Multilevel Interconnection Conference Proceedings, 1990, p. 226.

[33] D. Pramanik, "Characterization of Laser Planarized Aluminum for Submicron Double Level Metal CMOS Circuits", IEDM 89, p. 673.

[34] B.A. Boeck, K. Y. Fu, F. Pintchovski, N. Crain, S. Chen, and H. Chu, "Evaluation of Laser Planarized Second Aluminum for Semiconductor Devices", 1990 IEEE VLSI Multilevel Interconnection Conference Proceedings, 1990, p. 90.

[35] F.S. Chen, Y. S. Lin, G. A. Dixit, R. Sundaresan, C.C. Wei and F. T. Liou, "Planarized Aluminum Metallization for Sub-0.5 μm CMOS Technology", IEDM 90, 1990, p. 51.

[36] M. Taguchi, K. Koyama, and Y. Sugano, "Quarter Micron Hole Filling with SiN Sidewalls by Aluminum High Temperature Sputtering", 1992 IEEE VLSI Multilevel Interconnection Conference Proceedings, 1992, p. 219.

[37] T. Kikkawa, H. Aoki, E. Ikawa, and J. Drynan, "A quarter-micron Interconnection Technology using Al-Si-Cu/TiN Alternated Layers", IEDM 91, 1991, p. 281.

[38] J. Tao, K. K. Young, Nathan W. Cheung, and C. Hu, "Comparison of Electromigration Reliability of Tungsten and Aluminum Vias Under DC and Time-Varying Current Stressing", Proceedings of 1992 International Reliability Physics Symposium, P. 338-343.

[39] J. Tao, K.K. Young, N.W. Cheung, and C. Hu, "Electromigration Reliability of Tungsten and Aluminum Vias and Improvements Under AC Current Stress"

[40] P. Burggraaf, "Sputtering's Task: Metalizing Holes", Semiconductor International, Dec. 1990, p. 28.

[41] V. Comello, "A Manufacturable Sub-0.5 μm PVD Aluminum Plug Fill Process Developed", Semiconductor International, Feb. 1991, p. 13.

[42] M. J. Verkerk and W. A. M. C. Brankaret, "Effects of Water on the Growth of Aluminum Films Deposited by Vacuum Evaporation", Thin Solid Films, Vol. 139, 1986, p. 77.

[43] M. J. Verkerk and G. J. van der Kolk, "Effects of Oxygen on the Growth of Vapor-deposited Aluminum Films", Journal of Vacuum Science and Technology A, Vol. 4, No. 6, 1986, p. 3101.

[44] D. Pramanik and A.N. Saxena, "Aluminum Metallization for ULSI", Solid State Technology, Mar. 1990, p. 73.

[45] M.A. Nicolet and M. Bartur, "Diffusion Barriers in Layered Contact Structures", Journal of Vacuum Science. Technology, Vol. 19, 1981, p. 789.

[46] P.B. Ghate, "Metallization for Very-Large-Scale Integrated Circuits", Thin Solid Films, Vol. 93, 1982, p. 359.

[47] M. Wittmer, "Interfacial Reactions between Aluminum and Transition Metal Nitride and Carbide Film", Journal of Applied Physics, Vol. 53, 1982, p. 1008.

[48] R.N. Tait, S.K. Dew, T. Smy, and M.J. Brett, "Density Variations of Tungsten Films Sputtered over Topography", Journal of Applied Physics, Vol. 70, No. 8, p. 4295.

[49] D. Liu, T. Janacek, S.K. Dew, T. Smy, and M.J. Brett, "Computer Simulation of Collimated Sputtering of Titanium Thin Films over Topographic features", Journal of Applied Physics, Vol. 74, No. 2, 1993, p. 1339.

[50] R.N. Tait, S.K. Dew, T. Smy, and M.J. Brett, "Etching of Thin Metal Films Using a Ballistic Model", Journal of Vacuum Science and Technology A, Vol. 10, No. 4, 1992, p. 912.

[51] S.K. Dew, T. Smy, and M.J. Brett, "Simulation of Microstructure of Chemical Vapor Deposited Refractory Thin Films", Journal of Vacuum Science Technology B, Vol. 10, No. 2, 1992, p. 618.

[52] S.K. Dew, *Processes and Simulation for Advanced Integrated Circuit Metallization*, Ph.D. thesis, Department of Electrical Engineering, University of Alberta, Edmonton, 1992.

[53] S.K. Dew, T. Smy, and M.J. Brett, "Simulation of Elevated Temperature Aluminum Metallization Using SIMBAD", IEEE Transaction of Electron Devices, Vol. 39, No. 7, 1992, p. 1599.

[54] W. Tice and G. Slusser, "Relationship of Ambient deposition Conditions to Formation of Thermally Activated Voids in Al/Si interconnects", Journal of Vacuum Science Technology B, Vol. 8, No. 1, 1990, p. 106.

[55] R.S. Nowicki, "Influence of Residual Gases on the Properties of DC Magnetron Sputtered Aluminum-Silicon", Journal of Vacuum Science Technology, Vol. 17, No. 1, 1980, p. 384.

[56] J.F. O'Hanlon, "Vacuum Systems For Microelectronics", Journal of Vacuum Science and Technology A, Vol. 1, No. 2, 1983, p. 228.

[57] J. F. O'Hanlon, *A User's Guide to Vacuum Technology 2nd ed.*, Wiley, New York, 1989.

[58] M. Inoue, K. Hashizume, and H. Tsuchikawa, "The properties of Aluminum Thin Films Sputter Deposited at Elevated Temperatures", Journal of Vacuum Science Technology A, Vol. 6, No. 3, 1988, p. 1636.

[59] S.R. Wilson, J.L. Freeman, and Jr. C.J. Tracy, "A Four-Metal Layer, High Performance Interconnect System for Bipolar and BiCMOS Circuits", Solid State Technology, Nov. 1991, p. 67.

[60] W.R. Runyan and K.E. Bean, *Semiconductor Integrated Circuit Processing Technology*, Massachusetts, Addison-Wesley, 1990.

[61] S.P. Murarka, "Metallization", VLSI Technology 2nd ed., edited by S.Z. Sze, McGraw-Hill, New York, 1988, p. 375.

[62] C.R. Tottle, *An Encyclopaedia of Metallurgy and Materials*, Great Britain, Macdonald and Evans, 1984.

[63] D. Liu, S.K. Dew, M.J. Brett, T. Janacek, and T. Smy, "Properties of Titanium and Aluminum Thin Films Deposited by Collimated Sputtering", Thin Solid Films, Vol. 236, 1993, p. 267.

[64] X. Gui, W.C. Wu, and G.B. Gao, "An Improved Model of Thermal Stresses in Power Transistors", Acta Electronica Sinica, Vol. 14, No. 3, 1986, p. 123.

[65] J.A. Thornton and D.W. Hoffman, "Stress-Related Effects in Thin Films", Thin Solid Films, Vol. 171, 1989, p. 5.

[66] H. Ono, Y. Ushiku and T. Yoda, "Development of a Planarized Al-Si Contact Filling Technology", 1990 IEEE VLSI Multilevel Interconnection Conference Proceedings, 1990, p. 76.

[67] G. Carter, "The Influence of Surface Diffusion on Topography Development of an Amorphous Solid During Sputtering", Journal of Material Science, Vol. 11, 1976, p. 1091.

[68] G. Neumann, W. Hirschwald, "The Mechanisms of Surface Self Diffusion", Z. Physik. Chen. Neue Folge, Vol. 81, 1972, p. 176.